The 1956 eruption of Bezymianny volcano (Kamchatka). Part II - Magma dynamics and timescales from crystal records

Lea Ostorero[1,2*], Georges Boudon[1], Hélène Balcone-Boissard[3], Caroline Martel[4], Saskia Erdmann[4], Daniel J. Morgan[5], Alexander Belousov[6], Marina Belousova[6], Vesta Davydova[7], Thiebaut d'Augustin[3]

[1]Université Paris Cité, Institut de physique du globe de Paris (IPGP), CNRS, F-75005 Paris, France

[2]Now at Department of Earth and Environmental Sciences, University of Milano-Bicocca, Milan, Italy

[3]Institut des Sciences de la Terre de Paris (ISTeP), UMR 7193, CNRS-Sorbonne Université, Paris, France

[4]Institut des Sciences de la Terre d'Orléans (ISTO), UMR 7327, Université d'Orléans-CNRS/INSU-BRGM, Orléans, France

[5]Institute of Geophysics and Tectonics, School of Earth & Environment, University of Leeds, Leeds LS2 9JT, UK

[6]Institute of Volcanology and Seismology, 9 Piip Boulevard, Petropavlovsk-Kamchatsky, 683006, Russia

[7]Lomonosov Moscow State University, Geological Departments, Leninskii Gory, 1, 119191 Moscow, Russia

Corresponding author: Lea Ostorero
Email: leaemma.ostorero@unimib.it
ORCID: 0000-0002-8279-6596

Acknowledgments

We would like to thank S. Hidalgo for her help with sample preparation, O. Boudouma and S. Borensztajn for SEM imaging and E. Delairis for preparing the thin sections; additionally, we would like to thank M. Fialin and N. Rividi for assistance during the EMP analyses. C. M. and S. E. would like to thank P. Benoist and S. Janiec for sample preparation and help with the SEM analyses. All the authors are grateful to A.C. Laurent for designing the framework of the final figure. We thank L. Loïodice for participating in the study of orthopyroxene crystals during her Master 1 thesis, as well as L. Corrotti and E. Delhaye for their help in the preparation of magnetite mounts during their bachelor internships. The authors are grateful to an anonymous reviewer and to E. Mutch for their insightful comments that improved the manuscript, and to the associate editor J. H. Scarrow for the careful editorial handling. This project was funded by Université Paris Cité, Institut de physique du globe de Paris (IPGP) (L. Ostorero's doctoral grant from the French Ministry of Higher Education and Research and Innovation) and the ANR V-Care project (ANR-18-CE03-0010; coordinator: G. Boudon). C. M. and S. E. benefited from the EQUIPEX PLANEX project (ANR-11-EQPX-0036; B. Scaillet), the LABEX VOLTAIRE project (ANR-10-LABX-100-01; B. Scaillet), and the expertise and facilities of the Platform MACLE - CVL co-funded by the European Union and Centre-Val de Loire Region (FEDER).

Abstract

Laterally directed blasts are explosive events following a major sector collapse of a volcano, with the potential for devastating areas of several hundred km^2, due to powerful dilute and turbulent pyroclastic density currents. The catastrophic flank collapse on 30 March 1956 of Bezymianny (Kamchatka, Russia) was the climactic phase of the first historical magmatic eruption of this volcano, after 1000 years of dormancy. Magma stored in a cryptodome was depressurized by a sector collapse, generating a laterally directed blast immediately followed by pumiceous concentrated pyroclastic density currents. By combining petrological data from Bezymianny plumbing system and temporal constraints from orthopyroxene, magnetite, and amphibole chronometers, we tracked magmatic processes over twelve years prior to the eruption, followed by magma ascent to a shallow reservoir and a heating process at least three months before the eruption. Magma was last stored in a cryptodome at least two months before the climactic phase of the eruption. Evidencing magma dynamics of a few months to a few years

before major flank collapses and laterally directed blasts thus represent valuable information for volcanic risk mitigation (as it also occurred at Mt St. Helens).

Keywords: laterally directed blast, diffusion chronometry, orthopyroxene, magnetite, amphibole

Introduction

In volcano monitoring, key issues at stake are the uncertainties regarding the time of onset of an eruption, from volcanic unrest signals to the eruption. The time window between these two phenomena is a major field of research, as it can potentially threaten citizens lives and property and impact them on a large scale. To this end, crystals are powerful tools because they can be used as petrological clocks and are activated when magma storage conditions change (Anderson 1984; Streck 2008; Giacomoni et al. 2014; Petrone and Mangler 2021) such as during magma injection, magma mixing, or crystallization processes (Hawkesworth et al. 2004; Costa et al. 2020; Costa 2021; Petrone and Mangler 2021). After magmatic perturbations, crystals may grow rims with different compositions (called "zonations"). Multiple-zoned crystals with complex textures can form, recording the complexity of magmatic processes. With time, the crystal chemistry progressively returns to equilibrium by diffusion until eruption stops the diffusion process. Few studies have modelled diffusion in multiple minerals from the same eruption (Chamberlain et al. 2014; Singer et al. 2016; Cooper et al. 2017; Flaherty et al. 2018; Fabbro et al. 2018; Shamloo and Till 2019; Magee et al. 2020; Brugman et al. 2022; Kahl et al. 2023) or modelled the timescale given by more than one compositional boundary (Kahl et al. 2011; Druitt et al. 2012; Petrone et al. 2016, 2018; Rout et al. 2020). Combining diffusion timescales from multiple mineralogical chronometers and multiple layers permits us to obtain several independent timescale estimates and timescales of multiple diverse processes leading up to eruption, and thus unprecedented temporal information on pre-eruptive magmatic processes (Chamberlain et al. 2014; Fabbro et al. 2018). This type of study is particularly important for eruptions of arc volcanoes, which are highly dangerous due to the commonly evolved compositions and therefore viscous nature of the magmas and their elevated volatile contents prone to erupt explosively. A type of explosive eruption that has been understood in the last decades is that of those which are due to flank-collapse events. Flank collapses, following the injection of a magma mass in the flank of a volcano can produce powerful explosions with a significant laterally-directed component, that can generate devastating, high energy pyroclastic density currents (Voight 1981; Voight et al. 1981; Glicken 1998; Belousov et al. 2007). Despite their relatively small volumes of erupted magma (< 1 km^3), these eruptions have led to complete devastation in areas of up to hundreds of square kilometers (Belousov et al. 2007). The term of these eruptions (directed blast) was born following the 1956 flank collapse eruption of Bezymianny in Kamchatka, based on observations at a large distance by Gorshkov (1959). At the time, the eruption was misinterpreted, as the debris avalanche (the phenomenon was absolutely unknown then) and the laterally directed explosion were described together as a directed blast (Gorshkov and Bogoyavlenskaya 1965). The eruption of Mt St. Helens in 1980 (Voight 1981; Voight et al. 1981; Glicken 1998) and the detailed reinvestigation of the 1956 Bezymianny eruption by Belousov et al. (1996) contributed to a better understanding of the processes leading to directed blast eruptions.

The injection of magma in the form of a cryptodome into the eastern flank caused a large deformation during a growth period of approximately two to six months (Belousov et al. 2007), until its destabilization generated a debris avalanche and an open horseshoe-shaped edifice structure. The sudden depressurization of the gas-bearing magma of the cryptodome caused a laterally directed blast that resulted in the opening of the horseshoe shaped structure and destroying the entire eastern flank of the volcano (0.5 km^3 of debris avalanche) (Belousov and Bogoyavlenskaya 1988; Belousov 1996; Belousov and Belousova 1998; Belousov et al. 2007). The laterally directed blast was immediately followed by pumiceous concentrated pyroclastic density currents (C-PDC) (Belousov 1996), with a scenario similar to the 1980 eruption of Mt St. Helens (Lipman and Mullineaux 1981; Criswell 1987).

Predicting the date, style, and damage extent of these violent eruptions is still impossible but understanding the pre-eruptive processes controlling these devastating eruptions is necessary to progress toward a better risk assessment, which is particularly important for densely populated areas (such as Lassen volcanic center (Ewert et al. 2018) or Mount Lamington (Belousov et al. 2020)). The 1956 eruption of Bezymianny occurred in an area without a permanent settlement, and therefore had a limited direct impact on local population, however, this eruption provides an opportunity to investigate the changes that occurred in the magmatic system in the years preceding the flank collapse through petrological investigations.

Few timescale constraints have been estimated prior to Bezymianny 1956 eruption. A magma injection was thought to have occurred less than two months before the eruption (Plechov et al. 2008) and the magma leading to the post-blast pumiceous C-PDC was inferred to be last and transiently stored for at least 40 days between ~2-4 km (50-100 MPa, 890-930 °C) (Shcherbakov et al. 2013).

We aim to answer the following main questions:

(1) Which magmatic processes occurred before the 1956 eruption of Bezymianny?
(2) On which timescales before eruption did the magmatic processes take place?

To these aims, we combined the analysis of pre-eruptive timescales using different minerals (orthopyroxene, magnetite and amphibole).

Building on a companion paper on the architecture of the storage system prior to the climactic phase of the 1956 eruption of Bezymianny (Martel et al. accepted), we propose a time-constrained scenario of pre-eruptive magma dynamics from a deep reservoir (> 200 MPa) to a shallow reservoir (~50-100 MPa) up to the cryptodome (< 25 MPa).

Geological context and the 1956 flank collapse of Bezymianny

Bezymianny (2886 m, above sea level) is a Pleistocene andesitic volcano on the Kamchatka Peninsula (Braitseva et al. 1991; Girina 2013; Turner et al. 2013; Mania et al. 2019), where the Pacific plate subducts under the Kamchatka-Okhotsk continental block (~8 cm/yr) (DeMets 1992). Bezymianny is part of the Klyuchevskoy volcanic group (Braitseva et al. 1995; Levin et al. 2002; Journeau et al. 2022) and is located in the Central Kamchatka Depression, a region with the most magma-producing arc volcanoes on Earth (**Fig. 1**; **Supplementary Fig. 1**). Between 2.4-1.7 ka and 1.35-1 ka BP, major eruptive activity occurred at Bezymianny (Braitseva et al. 1991; Mania et al. 2019). Pre-historic eruptive activity formed lava flows, extrusive lava domes and extensive pyroclastic density current deposits, with volcanic activity intermitted by long phases of dormancy (Braitseva et al. 1991; Girina 2013; Turner et al. 2013). The last repose period of the volcano was from 1000 years BP to 1955 AD (Braitseva et al. 1991; Turner et al. 2013). The magma compositions ranged from basaltic andesite to dacite (Almeev et al. 2013).

1956 flank collapse and recent eruptions

After 23 days of intense seismic swarms, which began on 29 September 1955, the first historical eruption of Bezymianny started on 22 October 1955 (**Fig. 2a**) (Gorshkov 1959; Tokarev 1981, 1985). The eruption commenced with a preclimactic phase (the phase preceding a large eruptive phase or climactic phase) with explosive activity (probably phreatic to phreatomagmatic explosions (Belousov et al. 2007)) from within a new crater, with frequent ash explosions characterized by plumes rising as high as > 6 km (Gorshkov 1959; Belousov and Bogoyavlenskaya 1988). Eruptive activity diminished by 21 November. It is not sure if the accumulation of volcanic deposits due to the phreatic eruptions of the preclimactic phase formed a cone in the crater or if a lava dome may have grown slowly in the new crater, as observations conditions were difficult at the time (overflight on 25 January 1956). Simultaneously, a batch of magma started to intrude the eastern flank of the volcano (cryptodome), as the southeastern slope of the cone was slowly uplifted (by as much as 100 m, visible in photographs from February 1956) (Belousov and Belousova 1998; Belousov et al. 2007) (**Fig. 2c**). Later models considered that magma did not reach the surface before March 1956 and that all the deformations (on the flanks and of the crater) represented an uplift of old volcanic rocks that composed a plug, which was later ejected by the blast (**Fig. 2b**) (Gorshkov and Bogoyavlenskaya 1965; Belousov 1996). Until March 1956, weak explosions with ash plumes took place (up to 3 km high) (Gorshkov 1959).

On 30 March 1956, the climactic phase of the eruption began unexpectedly during a general weakening of volcanic and seismic activities (Gorshkov 1959) (**Fig. 2d**). The collapse of the highly deformed southeastern flank of the volcano generated a 0.5 km^3 debris avalanche that rushed down the flank of the volcano and its surroundings at a speed of ~60 m/s, covering an area of 36 km^2 and leading to the opening of a large horseshoe-shaped crater of 1.7x2.8 km (Belousov and Bogoyavlenskaya 1988; Belousov and Belousova 1998; Belousov et al. 2007). Unroofing the cryptodome, the flank-collapse triggered a catastrophic laterally directed blast toward the southeast, that led to the formation of a violent PDC (**Fig. 2**). This diluted and turbulent PDC with an average effective temperature of about 250 °C destroyed an area of ~500 km^2, travelling with a velocity of more than 100 m/s. The volume of the deposits was estimated to be 0.2-0.4 km^3 (Belousov 1996; Belousov et al. 2007). Following this explosion, the depressurization of the conduit triggered an explosive phase that produced a boiling-over pumiceous C-PDC with a volume of 0.5 km^3 (Belousov and Bogoyavlenskaya 1988; Belousov 1996; Turner et al. 2013). The blast-generated PDC and the post-blast pumiceous C-PDC jointly produced a convective ash cloud of 34-38 km high, which generated an extensive airfall deposit (0.2-0.3 km^3) to the north (Belousov and Bogoyavlenskaya 1988; Belousov 1996; Turner et al. 2013) (**Fig. 1b and 2; Supplementary Fig. 1**). The total volume of the eruptive products was between 0.9-1.2 km^3 (from the blast, post-blast pumiceous C-PDC and ash fallout deposits) (Belousov 1996).

The 1955-1956 eruption was immediately followed by a phase of intermittent lava dome growth that continues until now. The lava dome growth is accompanied by frequent lava dome collapses and strong Vulcanian explosions that produce moderate scale block-and-ash flows on average twice a year (Girina 2013; Turner et al. 2013). Products of this post-climactic activity are of progressively more mafic compositions (**Fig. 2**) (Turner et al. 2013; Davydova et al. 2022). It has been interpreted that the dome-forming eruptions from 2006 to 2012 were triggered by regular injections of hot volatile-saturated magma into the shallow magma storage zone (Davydova et al. 2017).

The volcano then remained dormant between September 2012 and December 2016 (Mania et al. 2019). Since December 2016, several explosive eruptions have occurred (Davydova et al. 2022; Global Volcanism Program 2023).

Magma plumbing system architecture prior to the 1956 flank collapse and climactic phase

Bezymianny's magma plumbing system architecture, intensive parameters and magmatic processes prior to the 1956 eruption have been constrained by several petrological and experimental studies (Kadik et al. 1986; Plechov et al. 2008; Almeev et al. 2013a,b; Shcherbakov et al. 2013), including our companion paper (Martel et al. accepted). These studies suggest mid- to upper-crustal magma storage at three main levels with magma and melt recharge.

Particularly, Martel et al. (accepted) investigated the pressure (depth) and temperature conditions of the plumbing system beneath Bezymianny from a multiphase petrological point of view from blast clasts and Plinian pumices from the climactic phase of the 1956 eruption. Using thermobarometry in amphiboles, melt inclusions, glass compositions, looking at microlites textures and compositions, and phase assemblage, a three-level magma storage architecture was found: (1) A deep magma reservoir at pressures of ≥ 200-350 MPa and depths of ≥ 8-13 km (using a magma density of 2650 $kg.m^{-3}$). The magma of the deep reservoir had roof conditions of ~850 °C, considering the uncertainties (840-865 ± 16 °C) and melt H_2O concentrations of ~4.5-6.7 wt%, with a stable phenocryst assemblage of plagioclase, amphibole, Fe-Ti oxides, orthopyroxene, and accessory minerals that records mixing between two magmas. A minor amphibole population recorded deeper and hotter storage areas, indicating crystallization at higher pressures of 280-700 MPa, temperatures of 850-990 ± 33 °C and melt H_2O concentrations of ~5.4-8.1 wt%. (2) A shallow reservoir at pressures of ~50-100 MPa and depths of ~2-4 km at a temperature of ~900 °C (850-925 °C; from the stability conditions of quartz), where amphibole partly decomposed (developing glass-rich reaction rims) and microlites, including quartz, crystallized. (3) A subsurface cryptodome at pressures of ≤ 25 MPa and depths of < 1 km. At temperatures ≥ 900 °C, amphibole decomposed (developing glass-poor reaction rims) and cristobalite formed. The magma that fueled the 1956 eruption was derived from the deep reservoir, but was intermittently stored at shallow level and/or subsurface level (cryptodome) en route to the surface. Vesiculated and dense clasts of the lateral blast were the products of magma temporarily stored first in the shallow reservoir and then in the subsurface cryptodome, whereas pumices from the post-blast C-PDC of the eruption were generated by magma temporarily stored only in the shallow reservoir. A pre-eruptive deep magma injection of a hot and more mafic magma is likely to have occurred in the deep reservoir, explaining a microlite nucleation event and An-rich compositions (Martel et al. accepted). Using seismic tomography, Koulakov et al. (2017, 2021) have also inferred current magma storage and source zones at mid crustal level (10-15 km) as well as at shallow level (3 km depth) and finally at very shallow level at ~1-2 km depth within the edifice of Bezymianny, in agreement with petrographic studies on December 2017 samples. Furthermore, earthquakes during eruptions at Bezymianny since 1999 characteristically extended from the surface to a depth of approximately 6 km, confirming the presence of a magma reservoir at mid-crustal depth (Fedotov et al. 2010; Thelen et al. 2010). It has also been proposed that Bezymianny, Klyuchevskoy and Tolbachik volcanoes derive their magmas from a common storage zone at >30 km depth (Koulakov et al. 2013, 2017, 2020, 2021; Shapiro et al. 2017).

Methods summary

Field sampling and sample preparation

Samples were collected in 2019 during a field campaign in Kamchatka, which targeted deposits of the laterally directed blast (called "blast" further down) and post-blast pumiceous C-PDC of the 1956 climactic phase (**Supplementary Table 1;** see **Supplementary Note**) (see Belousov and Belousova 1998).

Our study focused on orthopyroxene, magnetite and amphibole phenocrysts, which were present in all the samples. Rock mounts were prepared for eleven selected samples, comprising relatively dense blast clasts, vesicular and highly vesiculated blast clasts, and post-blast C-PDC pumices to characterize textural relations and for all analyses of amphibole crystals (**Supplementary Table 1**). Vesicular samples were also crushed using a jaw crusher and sieved for individual crystal investigations (see **Supplementary Note; Supplementary Table 1**). The phenocrysts were then handpicked from three size fractions, where they were most abundant (500-315 µm, 315-250 µm, 250-125 µm) (see **Supplementary Note**). Crystal mounts were polished up to 0.3 µm. Orthopyroxene crystals were oriented optically with the c-axis in the north-south direction (showing light brown colors) and polished to expose their crystal cores to prepare them for core to rim analyses and subsequent diffusion modelling, following other studies in this approach (e.g., Kilgour et al. 2014; Solaro et al. 2020; Ostorero et al. 2021, 2022; Metcalfe et al. 2021) (**Supplementary Note**).

Textural and compositional characterization

All the crystal mounts were characterized using Scanning Electron Microscopes (SEM): a Zeiss Supra 55VP (Sorbonne Université, ISTeP, Paris), a Carl Zeiss EVO MA10 SEM at the PARI platform at IPGP (Université Paris Cité) and a Merlin Compact ZEISS at ISTO using an acceleration voltage of 20 kV and a beam current of 8 nA. Overview back-scattered electron (BSE) images were acquired for the rock mounts and for the crystal mounts with greyscale variations to identify zoned orthopyroxene and magnetite. Higher magnification and resolution images of orthopyroxene zoned crystals were subsequently taken for diffusion modelling and intercalibration with profiles of compositional point analyses. Magnetite crystals with melt inclusion-rich zones separating the core and rim zones were also identified using the SEM (Boudon et al. 2015) (**Supplementary Note**).

Profiles of compositional point analyses were acquired for zoned orthopyroxene and magnetite using electron microprobe micro-analyzers (EMP): a CAMECA SX-Five and a CAMECA SX-100 (Service Camparis, Paris), operated at an acceleration voltage of 15 kV, a beam current of 10 nA, a focused beam of 2 µm and 2 µm steps along profiles ~60-200 µm in length (**Supplementary Note** for more details). For apparently unzoned orthopyroxene crystals, four points were measured across the crystal to confirm homogeneous compositions (**Supplementary Note**).

Timescale constraints

Interdiffusion timescales were modelled for zoned crystals that showed multiple compositional boundary layers or "bands" of different compositions, which record crystallization under different conditions resulting from open-system magmatic processes (Costa et al. 2020; Petrone and Mangler 2021; Chakraborty and Dohmen 2022). The timescales were modelled in AUTODIFF adapted for orthopyroxene (AUTODIFF_opx) and magnetite crystals (AUTODIFF_mgt). Demo versions of AUTODIFF_opx and AUTODIFF_mgt can be found in the **Supplementary Data** (**Supplementary Data 1 and 2**).

The timescales of magmatic processes can be estimated by using Fick's second law (Fick 1855) on compositional profiles by determining the initial conditions, boundary conditions and (inter) diffusivity of the elements of interest (Costa et al. 2020). The ionic (inter) diffusivity depends on several parameters, such as the chemical composition of the crystals (X_i; molar fraction of the mineral constituent element), temperature (T in K), pressure (P in Pa), oxygen fugacity (fO_2) and water fugacity (fH_2O) (Costa and Morgan 2010; Costa et al. 2020) (see **Online Resource 1**; **Supplementary Note**).

The main assumption is that the initial profile between the two compositional zones follows a step function, while the boundary conditions are open, based on the method subsequently used by other studies (Couperthwaite et al. 2020; Solaro et al. 2020; Ostorero et al. 2021, 2022). For orthopyroxene, the Fe-Mg interdiffusion profiles were modelled in one dimension, across the c-axis and parallel to the b-axis of the crystals (Allan et al. 2013; Couperthwaite et al. 2020), using the parametrization of the interdiffusion coefficient D of Fe and Mg in orthopyroxene (Ganguly and Tazzoli 1994). D has been defined without an oxygen fugacity fO_2 dependence in equation (1) (Ganguly and Tazzoli 1994):

$$\log D = -5.54 + 2.6X_{Fe} - \frac{12530}{T} \quad (1)$$

For magnetite, Ti diffusion magnetite was characterized by using the diffusion relationship constrained by Aragon et al. (1984), described in equation (2):

$$D^*_{Ti} = D^0_0 e^{-\left(\frac{E_{0\cancel{a}}}{RT}\right)} + D^0_V e^{-\left(\frac{E_v}{RT}\right)} f_{O_2}^{2/3} - D^0_I e^{-\left(\frac{E_I}{RT}\right)} f_{O_2}^{-2/3} \quad (2)$$

For T of interest and fO_2 of interest, where $D_0^0 = 8.2 \times 10^{-3}\ \mathrm{cm^2/s}$; $D_v^0 = 1.75 \times 10^{-12}\ \mathrm{cm^2}$ (s $\mathrm{atm}^{2/3}$); $D_I^0 = 3.9 \times 10^{-6}$ ($\mathrm{cm^2\ atm}^{2/3}$)/s; E_0= 60 kcal/mol; E_v = -28 kcal/mol and E_I = 159 kcal/mol.

The temperature is one of the main parameters influencing the timescales. For both orthopyroxene and magnetite, we used the temperatures determined for the deep and shallow reservoir of Bezymianny by Martel et al. (accepted). From glass compositions, thermobarometry of amphibole (Higgins et al. 2022) and looking at microlites and phase assemblages, the temperatures and uncertainties were estimated to be of ~850 ± 50 °C for the deep reservoir and ~900 ± 50 °C for the shallow reservoir where the magma at the origin of the blast and pumiceous C-PDC resided (Martel et al. accepted). For magnetite, the oxygen fugacity of ~1.5 above NNO was used (**Supplementary Table 2**; **Supplementary Fig. 2-3**) (average from the highly variable oxygen fugacity determined from amphiboles from the main population of the shallow reservoir: ~ΔNNO to ~ΔNNO+2.6; Martel et al. accepted). Timescales in multiple-zoned crystals have been modelled in several of their internal bands or external rims when possible. The bands were modelled independently, as AUTODIFF is not handling multiple-zoned profiles (not handling multi-steps) and as the diffusion timescales were not always modelled on successive bands (e.g. timescales modelled from B1 to B2 and B3 to B4 but not on B2 to B3) (**Supplementary Table 3; Supplementary Note**). As most of the modelling is undertaken at 900 °C, there is no differential response between core residence and rim residence in most cases, and a multi-step correction is not necessary (see Results). More details on the Fe-Mg interdiffusion modelling for orthopyroxene, the choice of diffusion coefficients, Ti diffusion modelling for magnetites and the temperatures used to estimate the timescales as well as the uncertainties can be found in the **Supplementary Note** (**Supplementary Table 2; Supplementary Fig. 2-3**). The method to calculate the uncertainties associated to the orthopyroxene timescales using a Monte-Carlo simulation can be found in **Supplementary Data 3**. The method of timescales estimation from amphibole rims thicknesses is also explained in the **Supplementary Note**.

Results

In this study, we used 19 andesitic samples from the climactic phase of the Bezymianny 1956 eruption (ten clasts from the blast and nine pumices from the post-blast C-PDC) (**Supplementary Table 1; Supplementary Fig. 4**). The mineral assemblage of the clasts from the blast and pumices from the post-blast C-PDC (written as C-PDC pumices in the rest of the manuscript) is identical and consists of plagioclase, amphibole, orthopyroxene and magnetite, forming pheno- and micro-phenocrysts (< 100 µm in length) (**Supplementary Information on the Methods**).

Phenocryst textures and compositions

Orthopyroxene

Zonation types

Orthopyroxene crystals are mostly zoned (alternative bands of different compositions). Based on SEM images, single-zoned orthopyroxene crystals were identified, as having either a normal-zoned rim, with a Mg-rich core (darker zone on a grayscale image) and an Fe-rich rim (rim-ward decreasing Mg#), or a reverse-zoned rim (with an Fe-rich core and a Mg-rich rim; rimward increasing Mg#) but also multiple-zoned orthopyroxene crystals (**Fig. 3; Supplementary Fig. 6-7**). The multiple-zoned orthopyroxene crystals have two or more intermediate zoning bands before an external rim. The multiple zonations exhibit an oscillating pattern, with Mg# increasing and then decreasing with intermediate plateaus of a few µm (from 2 to 50 µm) (**Fig. 3-4; Supplementary Fig. 6-7**). Some orthopyroxene crystals also show Al sector zoning (**Supplementary Fig. 5**).

A large number, i.e. 1091 orthopyroxene crystals from the blast and 1217 orthopyroxene crystals from C-PDC pumices were mounted in epoxy and characterized by BSE imaging. The orthopyroxene crystals of the blast and C-PDC pumices include a majority of zoned orthopyroxene (73-87 % and 84-89 %, respectively), with a predominance of multiple-zoned orthopyroxene crystals (73-93 % and 54-91%, respectively) (**Fig. 4**). Some fractions show multiple-zoned orthopyroxene crystals with more than five bands (39-81 % for the blast) (**Supplementary Fig. 7**). Combining all the size fractions, multiple-zoned orthopyroxene crystals with normal- and then reverse-zoned rims are dominant (36 % for the blast and 48 % for C-PDC pumices; **Fig. 4; Supplementary Fig. 7**).

Compositions

Among the 1091 and 1217 orthopyroxene crystals mounted, after selection of the best-preserved crystals (not fractured and showing well-defined bands), compositions of 38 and 55 zoned orthopyroxene crystals were investigated for the blast clasts and the C-PDC pumices, respectively, as well as 21 and 35 unzoned orthopyroxene crystals (**Fig. 5; Supplementary Fig. 8-10; Supplementary Data 4**). As a majority of multiple-zoned crystals was identified both in the blast and C-PDC pumices orthopyroxene crystals cargo (75 and 62 %, respectively; **Fig. 4**), multiple-zoned crystals were mainly analyzed by EPM for timescales modelling (100 % of the analyzed zoned crystals of the blast and 87 % of the analyzed zoned orthopyroxene in C-PDC pumices, while 13 % were in single-zoned crystals of the C-PDC pumices). Binary plots for major elements (CaO, FeO, MgO and MnO versus SiO_2) show common compositions for unzoned cores and cores of zoned orthopyroxene from blast and C-PDC pumices (**Supplementary Fig. 9**). The enstatite content ($En = \frac{Mg}{Mg+Fe}$) of unzoned orthopyroxene ranges from En_{63-66} for the blast and from En_{62-67} for the C-PDC pumices (± 0.9; **Fig. 5a-b; Supplementary Fig. 9-10**). For zoned orthopyroxene, the range of compositions is the same for the blast and C-PDC phase: En_{57-68} (**Fig. 5c-f; Supplementary Fig. 9-10**). The peaks of En content (%) for the cores of the zoned crystals plot around En_{64} for the blast and around En_{66} for the C-PDC pumices, whereas, for the bands of the zoned orthopyroxene crystals, two successive peaks of En_{62} and En_{66} are highlighted (**Fig. 5c-d; Supplementary Fig. 9-10**).

The same main En variations are identified in the bands of the zoned orthopyroxene crystals in both phases (**Fig. 5e-f**). In both phases, regarding the multiple-zoned orthopyroxene crystals and their external rims (called "N"), two populations of rims can be identified: normal-zoned rims (from En_{65-68} (N-1 band; 21-25% for the blast or C-PDC phase, respectively) to En_{58-64} (N rim; 14-29%)) or reverse-zoned rims (from En_{58-64} (N-1 band; 25-29%) to En_{65-68} (N rim; 21-36%)) (**Fig. 5e-f**). Furthermore, the En contents of the majority of multiple-zoned orthopyroxene crystals vary from En_{65-68} to En_{58-64} (normal zoning) and then from En_{58-64} to En_{65-68} (reverse zoning) (**Fig. 5e-f**). Few crystals show bands in the same En range (En_{65-68} for the blast or En_{58-64} in the C-PDC pumices).

Magnetite

Zonation types

Most of the magnetite crystals show concentric melt inclusion-rich zones (**Supplementary Fig. 3**), while few of them feature exsolution lamellae. Magnetite crystals in both blast and C-PDC pumice samples are reversely-zoned, with rare crystals being multiple-zoned (**Supplementary Fig. 3**).

Compositions

EMP analyses have been recalculated into ionic cations per formula unit and Fe^{2+} and Fe^{3+} ratio have also been constrained. In the blast clasts, the magnetite core compositions have 88-89 wt% FeO and 5-6 wt% TiO_2, while their rims have 84-89 wt% FeO and 6-9 wt% TiO_2 (**Fig. 6a; Supplementary Data 5**). In the C-PDC pumice samples, the magnetite cores have 87-90 wt% FeO and 5-7 wt% TiO_2, whereas their rims have 85-90 wt% FeO and 5.-10 wt% TiO_2 (**Fig. 6b; Supplementary Data 5**).

Amphibole

All amphibole phenocrysts in Bezymianny's 1956 eruption products are partly decomposed. Decomposition rims range from predominantly relatively thin external rims with homogeneous textures (Type-1 rims) to relatively thick external rims and pervasive amphibole decomposition with heterogeneous textures (Type-2 rims) and decomposition rims of intermediate type (Type-1 to Type-2 rims) (**Supplementary Fig. 11**). Pumices have predominantly amphibole with Type-1 reaction rims, but some have amphibole with thin Type-2 decomposition rims. Dense clasts from the blast have amphibole with thick, pervasive Type-2 decomposition rims (Martel et al. accepted). The compositions of the amphibole crystals are reported by Martel et al. (accepted), but there is no relation between amphibole composition and decomposition rim type.

Lifetime history of the phenocrysts

Temperatures were estimated from the composition of orthopyroxene crystals and their hosted melt inclusions from C-PDC pumices (Martel et al. accepted; d'Augustin 2021), which indicate equilibration at 930 ± 26 °C (equation 28a; Putirka 2008) (**Supplementary Table 2**). These calculated orthopyroxene-melt temperatures are comparable within uncertainties with temperatures constrained using amphibole and the phenocryst phase assemblage (Shcherbakov et al. 2013; Martel et al. accepted) (see **Methods**).

Thus, the temperatures determined by Martel et al. (accepted) of 850 ± 50 °C for the deep reservoir and 900 ± 50 °C for the shallow reservoir are the ones that were used for the diffusion timescales as they considered several thermometers and as they encompass the whole range of temperatures determined using other methods detailed before (see **Supplementary Note**).

Orthopyroxene timescales

Out of the transects analyzed in zoned crystals of the blast and of the C-PDC pumices, respectively, only the profiles with sigmoidal shapes (due to diffusion) were treated to derive timescale constraints (**Fig. 7; Supplementary Data 6**). These timescales are maximum timescales given that modelling was done from step initial conditions and as growth may produce non-sharp interfaces (**Fig. 7**). Thus, 45 and 52 profiles were modelled for orthopyroxene in the blast and post-blast pumiceous C-PDC, respectively (**Supplementary Data 6**). Five timescales were modelled on compositional profiles depicting En changes in the same En range (En_{58-64}) so the figures only show the timescales corresponding to compositional differences in different En ranges: from En_{58-64} to En_{65-68} or En_{65-68}-En_{58-64} (**Fig. 7-8; Supplementary Fig. 12; Supplementary Table 3**).

As introduced in the **Supplementary Note** and in the paragraph before, the temperature of 850 ± 50 °C (Martel et al. accepted) was used to model timescales on core to inner normal bands (for one band in the blast clasts and five in the C-PDC pumices) as we hypothesize that these normal zonations may have formed in the deep reservoir at lower temperature (**Fig. 8; Supplementary Data 6**). As the uncertainties associated to the temperatures are high, modelling the timescales with 900 or 850 °C stays in the same order of magnitude. The timescales have also been modelled for both external rims (rim N) and inner or intermediate bands (N-1 and N-2…), either normally or reversely zoned, with the same temperature of 900 ± 50 °C, as they must have formed at a higher temperature than the core and inner rims, in the shallower reservoir, even if the uncertainties on the temperatures of these two reservoirs overlap. The fO_2 conditions calculated from amphiboles by Martel et al. (accepted) could indicate oxidized conditions late in the magma history, that could also explain these reverse zoning patterns. In the entire dataset, only two crystals contain two boundaries that were modelled at different temperatures. An offline correction can be applied to account for differential residence (**Supplementary Data 6**). For Bezy8f_250_L6C3, the overall timescale drops from 128 days to 107, which is well within uncertainty. For Bezy9_250_L8C7g, the rim residence is very short compared to the core and the overall crystal core timescale shortens from 4484 days to 4477 days, which is not a significant change.

For both the blast clasts and C-PDC pumices, orthopyroxene-derived timescales of all bands indicate perturbation of the magma system a few years to days prior to eruption (**Fig. 8**; **Supplementary Fig. 12; Supplementary Data 6**). The timescales estimated for all the external rims N are mainly less than one year prior to the eruption, with the majority of timescales below 200 days (~ 6 months) (**Fig. 8**; **Supplementary Fig. 12; Supplementary Data 6**).

For the blast, the timescales of the external reverse-zoned rims N of the zoned orthopyroxene crystals range from ~11 months (327 (-227/+741) days) to 8 (-5/+17) days before the eruption, with the majority of the timescales below one month prior to the climactic phase (**Fig. 8c; Supplementary Fig. 12-13; Supplementary Data 6; Methods** for uncertainties). The same is observed for the external reverse-zoned rims N of the post-blast pumiceous C-PDC, apart from one profile indicating perturbation 2.3 (-2/+5) years before eruption (**Fig. 8b**). For the blast, external normal-zoned N rims give timescales between 11 months (334 (-225/+694) days) to a few days before the climactic phase but the data are limited (n = 6) (**Fig. 8a**). For the C-PDC pumices, the timescales of the external last N normal-zoned rims of orthopyroxene range from approximately 2 (-1/+4) years to a few days (5 (-3/+10) days) before the climactic phase (**Fig. 8b;d**). For normal-zoned inner (N-2) and N-1 bands in orthopyroxene crystals from the blast and C-PDC pumices, the calculated timescales are from 5 years (-4/+11) to 1 month (-25 days/+76 days) before the eruption, with a majority of the normal-zoned inner bands recording perturbations < 6 months prior to eruption (**Fig. 8b;d**). The inner reverse-zoned bands indicate formation between 128 days (-86/+263 days) and 3 (-2/+6) years before eruption (**Fig. 8**). For core-inner normal bands (using 850 ± 50 °C), the timescales are from 12 (-9/+100) years to 137 days (-114/+664 days) before the eruption (**Fig. 8**).

Magnetite timescales

Using the same temperature used for the orthopyroxene crystals of 900 °C (Martel et al. accepted), Ti diffusion timescales were modelled in the blast and C-PDC pumices (**Fig. 6c; Supplementary Data 7**).

Out of the 637 magnetite crystals in the blast and 644 in the C-PDC pumices, 10 and 31 profiles, respectively, were measured in unfractured magnetites with a well-defined inclusion ring (**Supplementary Data 7**). As a majority of reverse-zoned crystals was identified both in the blast and C-PDC pumices magnetite crystals cargo, reverse-zoned crystals were mainly analyzed by EPM for timescales modelling. For the blast, timescales modelled on reverse-zoned magnetite crystals are young, shorter than 180 days (6 months), with 60 % of the timescales ranging from 2-1 months (-26/+57 days; -12/+28 days, respectively) (**Fig. 6c; Supplementary Fig. 13; Supplementary Data 7**). For the C-PDC pumices, the timescales of the reverse-zonings are shorter than those of the blast, with timescales of less than two months prior to the climactic phase, with the majority ranging from 50 (-25/+56) days to (2 (-1/+2) days (**Fig. 6c; Supplementary Fig. 13; Supplementary Data 7**).

Only two timescales were modelled on the core to the inner reverse-zoned rim of multiple-zoned magnetite crystals in the blast and C-PDC pumices (of 47 (-18/+52) days and 8 (-4/+9) days, respectively) (**Fig. 6c; Supplementary Fig. 13**).

Amphibole decomposition rim thicknesses

Amphibole decomposition rims can be divided into two end-member types (referred to as Type-1 and Type-2) and intermediate types. Type-1 amphibole decomposition rims, which are present in vesiculated clasts of the blast and C-PDC pumices, are relatively glass-rich (~ ≤ 25 vol% glass) with minimum thicknesses of ~6-11 ± 2 µm (**Supplementary Fig. 11; Supplementary Table 4**). Their thicknesses are comparable to those of amphibole decomposition rims from other C-PDC pumices (~5-10 µm) from Bezymianny's 1956 eruption, which were determined by Shcherbakov et al. (2013). Type-2 amphibole decomposition rims, which are characteristic of dense clasts of the blast, are relatively glass-poor (≤ 5-10 vol% glass) and texturally heterogeneous, with minimum thicknesses of ~22-29 ± 2 µm (**Supplementary Fig. 11; Supplementary Table 4**). Their thicknesses compare to those of amphibole crystals from other dense clasts of the 1956 blast (~25-35 µm) characterized by Plechov et al. (2008). Intermediate type amphibole decomposition rims (≤ 20 vol% glass), which are characteristic of the vesiculated clasts of the blast, have less glass than the Type-1 rims and exhibit more extensive decomposition, with minimum rim thicknesses of ~9-16 ± 2 µm (**Supplementary Fig. 11; Supplementary Table 4**). Based on inferred equilibration pressures in the three reservoirs below Bezymianny (Martel et al. accepted) and data from decompression experiments (Rutherford and Hill

1993; Browne and Gardner 2006), probable decomposition rates were estimated for each type of amphibole: from 1.3-6 µm/day for Type-1, 0.5-1.5 µm/day for Type-2 and 0.5-2 µm/day for the intermediate type (**Fig. 9a**). Timescales derived from the rims thicknesses and decompression rates are discussed below (**Fig. 9b-d; Supplementary Table 4**).

Discussion

Martel et al. (accepted) suggests that the magma emitted during the post-blast pumiceous C-PDC was first stored in the deep storage area and then in the shallow reservoir. The magma at the origin of the blast was the same as the post-blast pumiceous C-PDC but it was stored in the deep and shallow reservoirs and finally in the cryptodome (Martel et al. accepted). As a result, our multi-mineral study of orthopyroxene, magnetite zonations and amphibole decomposition rims in the blast and pumiceous C-PDC samples provides insights into the timescales of the different magmatic processes taking place at these different storage levels.

Multi-step ascent evidenced by amphibole

Studies of amphibole decomposition rims formed by decompression can generally provide (1) depth-constrained timescales (i.e. constraints for residence outside the amphibole stability field), and (2) a screening tool for samples that are ideally studied in more detail by diffusion chronometry. Our analysis and previous work of Plechov et al. (2008) and Shcherbakov et al. (2013) show that Bezymianny amphibole decomposition rim thickness generally increases from pumice to vesiculated and to dense clasts of the blast. Our and previous work moreover show that the conditions of amphibole decomposition in Bezymianny's system (decomposition at < 100 MPa and > 850 to < 950 °C; Martel et al. accepted) closely compare to the conditions that have been experimentally explored by Rutherford and Hill (1993), Rutherford and Devine (2003), and Browne and Gardner (2006) (i.e. decomposition at < 130 MPa and 830-900 °C), thus permitting constraints on the natural system from the experimental decomposition rates. On the basis of this rationale, Plechov et al. (2008) and Shcherbakov et al. (2013) inferred that amphibole decomposition rims in pumices (~5-10 µm wide) and dense blast clasts (~25-35 µm wide), respectively, experienced magma storage for ~2 to 14 days and ~4 to 34 or 37 days outside the amphibole stability field (using the range of experimentally-constrained single-step and multi-step amphibole decomposition rates of Rutherford and Hill (1993) and Rutherford and Devine (2003)).

If compared to the entire range of experimentally constrained decompression rates (i.e. those of Rutherford and Hill (1993), Rutherford and Devine (2003), and Browne and Gardner (2006) with minimum to maximum rim development rates of 0.5-6 µm/day), then Type 1 amphibole rims in our pumice samples indicate decomposition for ~1 (± 0.3) to 22 (± 4) days, intermediate Type-1 to Type-2 rims in vesiculated blast clasts indicate decomposition for ~2 (± 0.3) to 32 (± 5) days, and Type-2 rims present in dense blast clasts indicate decomposition for ~4 (± 0.5) to ≥ 58 (± 8) days (**Fig. 9b**; "broad estimate" in **Supplementary Table 4**). For the Type-1 to Type-2 rims, similar timescales are thus calculated as by Plechov et al. (2008) and Shcherbakov et al. (2013), but they extend to overall larger durations (**Fig. 9**). However, tighter constraints can be derived, if we consider the different shallow, pre-eruptive storage conditions of magmas that formed the different types of amphibole decomposition rims in the dense blast clasts, vesiculated blast clasts, and pumice, respectively, considering pressure and temperature during amphibole rim formation (**Fig. 9b**; "best estimate" in **Supplementary Table 4**).Type-1 decomposition rims, which occur in pumice samples and highly vesiculated clasts with quartz microlites, are interpreted to have formed at ~50-100 MPa and > 850 to < 950 °C, where experimental amphibole decomposition rims mostly grow at rates of ~1.3 to 6.0 µm/day (**Fig. 9a**), thus likely indicating shallow magma storage for ~1.5 (± 0.3) to 8 (± 1.5) days (pumice and highly vesiculated clasts of the blast) (**Fig. 9b-d, Supplementary Table 4**) and ~1.0 (± 0.3) to 8 (± 1.6) days (pumiceous C-PDC). Intermediate type decomposition rims, which occur in vesiculated blast clasts with quartz microlites and rare, small cristobalite blebs, are inferred to have commenced decomposition at > 50 MPa and then continued to decompose at < 25 MPa also at > 850 to < 950 °C, where experimental amphibole decomposition rims mostly form at rates of ~0.5 to 2.0 µm/day (**Fig. 9a**). They thus likely indicate shallow magma storage for > 5 (± 1.0) and < 32 (± 5.2) days (**Fig. 9b-d**, **Supplementary Table 4**). Type-2 decomposition rims, which occur in dense blast clasts with large, ubiquitous cristobalite blebs, are inferred to have formed at < 25 MPa and ~900-950 °C, where experimental decomposition rims mostly grow at rates of < 1.5 µm/day (**Fig. 9a**), thus likely indicating storage in the subsurface cryptodome for > 15 (± 2.1) to > 58 (± 7.8) days (**Fig. 9b-d**, **Supplementary Table 4**). If temperatures increased indeed from magma in the shallow reservoir (> 850 to < 950 °C), where Type 1 rims formed, to magma in the cryptodome (~900-950 °C), where Type 2 rims formed (Shcherbakov et al. 2013; Martel et al. accepted), then the residence timescales of the cryptodome magma and the blast may be overestimated relative to those of the magma erupted from the shallow reservoir that generated pumice, but within our broad estimates (**Fig. 9**). We highlight that even though our best estimated amphibole rim timescales remain necessarily relatively broad (owing to limited experimental constraints for comparison), we posit that they nevertheless provide a record of critical events months to days prior to the catastrophic 30 March eruption, as detailed below.

Magmatic dynamics and timescales

Regarding orthopyroxene zonation types, an increase in En (reverse zoning) is mainly caused by heating with or without magma mixing with a hotter magma (Martel et al. 1999; Solaro et al. 2020). By contrast, an En decrease (normal zoning) may be related to a decompression process, mixing with a cooler magma or degassing (Martel et al. 1999; Frey and Lange 2011; Saunders et al. 2012; Kahl et al. 2013). For magnetite crystals, an increase in Ti can indicate a heating event, oxidation event or magma mixing (Devine et al. 2003).

We infer that for multiple-zoned orthopyroxene crystals, core to inner normal bands were formed in the deep reservoir, as the temperature was lower in this reservoir and then the intermediate bands to external rims of orthopyroxene crystals could have formed at higher temperatures, as also suggested by the zoning in magnetites. As specified before, the average temperature of the deep reservoir (850 ± 50 °C; Martel et al. accepted) was thus used to model the timescales recorded by the compositional transitions between orthopyroxene cores and inner normal bands of the multiple-zoned crystals, as they were likely formed in this reservoir (**Fig. 8; Supplementary Data 6**). An average temperature of 900 ± 50 °C was used to estimate all timescales for the intermediate and external rims of orthopyroxene and magnetite crystals, which are probably formed in the shallow reservoir (Martel et al. accepted) (**Fig. 6-8; Supplementary Fig. 2**). The interpreted timescales below are thus estimated using these temperatures.

Concerning orthopyroxene, approximately 80 % of the crystals are zoned, indicating that they experienced significant changes in magmatic crystallization conditions. The small proportion of unzoned orthopyroxene crystals from samples of both the blast and pumiceous C-PDC (20 %; **Fig. 4**) are interpreted to represent crystals that were in parts of the deep reservoir that did not experience a significant change in magmatic conditions (**Fig. 5**; **Supplementary Fig. 8-10**).

Timescales linked to the zoned crystals are from a few years to a few days, depending on the type of crystals, with longer timescales recorded by orthopyroxene crystals compared to magnetite crystals and amphibole decomposition rims (**Fig. 6-9**). These timescales estimated on different types of zonations are interpreted below in terms of processes occurring in the different reservoirs below Bezymianny, in the framework of the architecture determined by Martel et al. (accepted).

Deep reservoir

Several years before the climactic phase (4 (-3/+21) - 12 (-9/+100) years), perturbations in the deep reservoir occurred (~8-10 km), resulting in the formation of reverse- and normal-zoned inner bands in orthopyroxene crystals (associated with En changes characterized mainly between En_{65-68} and En_{58-64} or the reverse) (**Fig. 5; Fig. 7-8; Fig. 10a; Supplementary Fig. 12-13; Supplementary Data 6**). Slow magma convection in the same reservoir could have formed these different oscillating bands close in En content (Couch et al. 2001).

Then, from 2 (-1/+4) years to 5 months (-105/+321 days) before the climactic phase, degassing of the deep reservoir took place (**Fig. 10b**) (normal-zoned inner bands formed in the orthopyroxene of the blast and C-PDC pumices; **Fig. 8**). This degassing pattern is also supported by orthopyroxene-hosted melt inclusions where a CO_2 degassing trend was also highlighted (Martel et al. accepted). (c) Six months before the climactic phase, mixing in a thermally-zoned reservoir could have then formed reverse-zoned inner bands (**Fig. 8; Fig. 10c**).

Shallow reservoir

Then, from ~ 3 months before the eruption, part of the magma of the deep reservoir began to ascend to form the shallow reservoir (normal-zoned N-1 bands; **Fig. 8; Fig. 10d**). Furthermore, melt inclusion compositions, the presence of quartz, and the absence of cristobalite, have also traced magma migration from the upper part of the deep reservoir (200-300 MPa, ~850 °C) toward intermittent shallower storage at pressures of ~50-100 MPa (~2-4 km depth) (Martel et al. accepted). The injection of mafic melt in the deep reservoir, inferred by Martel et al. (accepted), could have occurred around this time triggering magma ascent from the deep reservoir to the shallow reservoir, forming An-rich microlites. This injection of a hotter and more mafic magma from below occurred without mixing, as the melts sampled by the melt inclusions and residual glasses are rhyolitic (Martel et al. accepted) and no resorption zones are recorded in orthopyroxene or magnetite crystals. Using whole-rock trace-element data, Turner et al. (2013) also inferred that a magma injection occurred at depth, suggesting magma recharge for the deep reservoir (**Supplementary Fig. 4**). From there on, a heating event was recognized approximately 3 months to a few days prior to the climactic phase in the blast clasts and C-PDC pumices during which external reverse-zoned rims formed in orthopyroxene and magnetite crystals (**Fig. 8; Fig. 10d**) (3 months (-95 days/+3 years) - 2 (-1/+4) days for orthopyroxene crystals and 166 (-82/+184) days - 2 (-1/+2) days for magnetite crystals; **Supplementary Data 7**), that could be due to heating from the mafic injection below. This injection was not accompanied by mixing in 1956, but the injected magma could have later mixed with the part of the magma staying in the deep reservoir and could explain the more mafic compositions of the lavas post-1956 (Turner et al. 2013).

Reverse-zoned crystals from the blast giving timescales from 3 to 2 months may have formed in this shallow reservoir, due to heating from the injection below (**Fig. 8b; Fig. 10d**). As shown by amphiboles, magma ascent from the deep reservoir to the shallow one occurred up to eight days before the climactic phase (Type-1 amphibole in C-PDC pumices and some clasts of the blast), during which time magma ascent may have critically increased overpressure (**Fig. 9c-d; Fig. 10e**).

Cryptodome

At the same time (~two to three months before eruption onset), magma ascent up to the shallow reservoir could have allowed the opening of fractures towards the surface. A large volume of magma is then injected into the south-east flank of the edifice, forming a cryptodome and a progressive deformation of the south-east flank (**Fig. 10d**). Indeed, the blast magma is cristobalite-rich (Martel et al. accepted). Furthermore, external normal-zoned orthopyroxene rims from the blast have timescales between 11 (-4/+23) months and one month (-15/+47 days) (**Fig. 8; Supplementary Data 6**), indicating magma decompression**.** Type-2 amphibole decomposition rims also recorded very shallow storage for 58 days (± 8 days) or more for magma that formed dense clasts in the blast (**Fig. 9; Supplementary Fig. 11**). This timescale is longer than that previously inferred (≤ 34-38 days (Plechov et al. 2008; Shcherbakov et al. 2013)), but is in agreement with observations of flank uplift in January and February 1956, thus approximately two months prior to the flank collapse and the generation of the blast (Belousov and Belousova 1998).

Some external reverse-zoned orthopyroxene and magnetite crystals of the blast giving timescales of a few days were likely formed by heating from the magma below (**Fig. 8; Supplementary Table 3; Supplementary Data 6-7**), as this study used individual orthopyroxene and magnetite crystals from relatively vesiculated clasts from the cryptodome (**Supplementary Table 1**). The cryptodome was probably zoned in temperature, with a colder crust that had denser and colder clasts, richer in cristobalite, as identified by Martel et al. (accepted) and Plechov et al. (2008) (**Fig. 10d-e**).

The external reverse zonings in orthopyroxene and magnetite crystals could also be formed by oxidation of magma by sulfur degassing during decompression (Jugo 2009; Gaillard and Scaillet 2014), as oxidizing conditions have been calculated (ΔNNO up to ~ΔNNO+2.6) for the magma (**Fig. 6-8**) (Martel et al. accepted). It has indeed been shown that Ca-experimental orthopyroxene crystals become richer in En when the oxygen fugacity increases for a given temperature and H_2O melt content (Martel et al. 1999). Orthopyroxene crystals from C-PDC pumices also show short timescales for reverse zonings, whereas they are stored deeper than the cryptodome, so a magma influx from the deep reservoir to the shallow one could have led to some heating in the shallow reservoir (**Supplementary Data 6**). Another explanation of this temperature increase could originate in degassing-driven crystallization releasing latent heat, as it was shown for hydrous magmas that decompress sufficiently slowly to allow crystallization based on Mt St Helens and Shiveluch (Kamchatka) melt inclusions (Blundy et al. 2006).

Furthermore, magma that formed vesicular clasts in the blast with intermediate type amphibole decomposition rims also continued to ascend from shallow to very shallow storage for less than 32 days before the climactic phase (**Fig. 9c-d; Fig. 10e**). These timescales agree with continued cryptodome growth and inflation of the volcanic edifice (Belousov and Belousova 1998).

If we consider the effect of our temperature assumption used for the modelling of the timescales, we can calculate the corresponding timescales. A higher temperature estimate (930 °C, for the pumiceous C-PDC from melt inclusions (Martel et al. accepted; d'Augustin 2021)) leads to shorter timescales (overall the timescales would be divided by 2; a maximum of 660 days compared to 1475 days using 900 ± 50 °C) (Martel et al. accepted) (**Supplementary Fig. 14**). However, the large uncertainties of the temperatures used to model the timescales overlap with the ones using 930 °C so the timescales would be of the same order of magnitude, around some years to days before the climactic phase.

Seismic data and comparison with the Mt St. Helens 1980 blast

Up to September 1955, in the Klyuchevskoy group, not a single earthquake with an epicenter close to Bezymianny was recorded (Tokarev 1981). Comparing the inferred magma dynamics to recorded seismic signals is challenging, as a significant portion of the deep seismic precursors likely went undetected. This could be due to the fact that only a single seismic station, located 42 km away from Bezymianny volcano, has been recording data since 1946 (seismic catalog in Russian: Tokarev 1981, 1985). Additionally, an active transcrustal magmatic system connects several volcanoes in the Klyuchevskoy group, with a well-developed magma reservoir currently located beneath Bezymianny. Consequently, the seismicity in this hot area might have been beyond the resolution of the instrumentation at the time, or the early ascent of magma could have been seismically silent within the ductile crust (Shapiro et al. 2017; Melnik et al. 2020; Journeau et al. 2022). The pre-eruptive seismic crisis from the end of September to October 1955 likely reflects reactivation of the system. The coordinates of the earthquakes could not be determined accurately due to the presence of only one seismic station (Tokarev 1981). The depths of the earthquakes were also not determined at the beginning of the crisis and the epicenters were constrained for the first time for the earthquake on 11 October, to be approximately 5 km deep in the area of Bezymianny (Gorshkov 1959). Therefore, the seismic crisis could have begun before, perhaps with some events occurring some years before the climactic phase, in relation to the first timescale recorded in the orthopyroxene zonings in the deep reservoir, or the early ascent could have been silent, as it occurs in Iceland with more mafic and less viscous magmas (Kahl et al. 2023). Indeed, for the 2021 Fagradalsfjall eruption, deep magmatic unrest preceded geophysical eruption precursors on the Reykjanes Peninsula by at least one year (Kahl et al. 2023).

Considering the early-warning signs for monitoring centers, these earthquakes were detected two months before the preclimactic phase of the eruption, and six months before the climactic phase, allowing to identify the location of the eruption, whereas Bezymianny was considered extinct (Gorshkov 1959).

For other directed blast eruptions, such as the 1980 eruption of Mt St. Helens (Lipman and Mullineaux 1981), which was of the same magnitude as the 1956 Bezymianny eruption and which devastated an area of comparable size 600 km^2 (500 km^2 for Bezymianny) (Belousov et al. 2007), pre-eruptive timescales constrained by orthopyroxene diffusion chronometry exist (Saunders et al. 2012). At Mt St. Helens, seismic swarms and deformation of the volcanic edifice mainly occurred two months before the flank collapse (Endo et al. 1981; Scandone et al. 2007; Saunders et al. 2012), with long-period earthquakes associated with degassing of magma occurring mainly one month before. Recharge or convective overturn of the magmatic system occurred a few months to a few years before the blast (4 months-10 years; 4 timescales) and was linked to deep seismicity some weeks before the blast (Saunders et al. 2012). No seismic records are available before 1980. The magma dynamics inferred for the 18 May 1980 eruption of Mt St. Helens are similar to what is inferred here for the 1956 Bezymianny eruption, with recharge or convective overturn of the magmatic system occurring approximately one year before the eruption and degassing (Saunders et al. 2012). These deformation patterns identified for both Bezymianny and Mt St. Helens two months before the blasts can be an early-warning sign of magma intrusion at shallow depths (> 100 m) (Scandone et al. 2007; Belousov et al. 2007) and pressurization of magma, which are also recorded in crystals. These timescales of early-warning signs could be useful for volcano monitoring research centers.

Conclusion

Directed blasts are threatening and understanding their pre-eruptive dynamics and timescales is of particular importance, especially if little unrest activity is detected prior to these events. Combining information from several petrological clocks provides additional insights into the pre-eruptive dynamics of these catastrophic eruptions. From orthopyroxene, magnetite and amphibole, multi-step magma ascent is inferred prior to the climactic phase of the 1956 eruption of Bezymianny. Twelve to two years before the eruption, self-mixing and degassing occurred in the deep reservoir. This reactivation was not recorded by seismic signals and can be important to interpret future eruptions. Then, more timescales are recorded in the two years before the climactic phase and at least three months before the eruption, magma ascended from a deep reservoir to a shallower one. A heating event linked to magma injection from below or degassing induced crystallization with possible oxidation could have contributed to the formation of reverse zonations. Magma then ascended very close to the surface, to form a cryptodome, as observed at the time. Here, we estimated the time between the onset of flank deformation by cryptodome growth and the climactic phase of the eruption to be at least three months, which must be considered in risk mitigation scenarios, as well as longer timescales. Unrest phases at gravitationally instable volcanoes with lava domes should thus be closely monitored, as lateral blasts can possibly occur.

Author contributions

L. O., G. B., H. B.B., C. M., S. E., A. B., M. B. and T. d'A. participated in the field mission in 2019 to Kamchatka (Russia) to collect all the samples characterized in this study. L.O. performed the data acquisition on orthopyroxene and magnetite crystals, prepared the figures and wrote the manuscript. S. E. collected, interpreted the amphibole data and wrote the initial versions of the parts on amphibole in the manuscript. D. M. provided the updated spreadsheets models of the diffusion timescales, the Monte-Carlo uncertainty simulation spreadsheet (**Supplementary Data 1-3**) and participated in the discussion of the data. L. O., G. B., H. B.B., C. M. and S. E. participated in the interpretation of the data and the writing of the manuscript text. All the authors reviewed the manuscript.

Statements and declarations

Competing interests: All the authors declare no competing interests.

References

Allan ASR, Morgan DJ, Wilson CJN, Millet M-A (2013) From mush to eruption in centuries: assembly of the super-sized Oruanui magma body. Contrib to Mineral Petrol 166:143–164. https://doi.org/10.1007/s00410-013-0869-2

Almeev RR, Kimura J-I, Ariskin A, Ozerov AY (2013) Decoding crystal fractionation in calc-alkaline magmas from the Bezymianny Volcano (Kamchatka, Russia) using mineral and bulk rock compositions. J Volcanol Geotherm Res 263:141–171. https://doi.org/10.1016/j.jvolgeores.2013.01.003

Anderson AT (1984) Probable relations between plagioclase zoning and magma dynamics, Fuego Volcano, Guatemala. Am Mineral 69:660–676

Belousov A (1996) Deposits of the 30 March 1956 directed blast at Bezymianny volcano, Kamchatka, Russia. Bull Volcanol 57:649–662. https://doi.org/10.1007/s004450050118

Belousov A, Belousova M, Hoblitt R, Patia H (2020) The 1951 eruption of Mount Lamington, Papua New Guinea: Devastating directed blast triggered by small-scale edifice failure. J Volcanol Geotherm Res 401:106947. https://doi.org/10.1016/j.jvolgeores.2020.106947

Belousov A, Voight B, Belousova M (2007) Directed blasts and blast-generated pyroclastic density currents: a comparison of the Bezymianny 1956, Mount St Helens 1980, and Soufrière Hills, Montserrat 1997 eruptions and deposits. Bull Volcanol 69:701–740. https://doi.org/10.1007/s00445-006-0109-y

Belousov AB, Belousova MG (1998) Bezymyannyi Eruption on March 30, 1956 (Kamchatka): Sequence of Events and Debris-Avalanche Deposits. Volcanol Seismol 20:29–47

Belousov AB, Bogoyavlenskaya GE (1988) DEBRIS AVALANCHE OF THE 1956 BEZYMIANNY ERUPTION. In: Kagoshima International Conference on Volcanoes, Japan. pp 460–462

Blundy J, Cashman K, Humphreys M (2006) Magma heating by decompression-driven crystallization beneath andesite volcanoes. Nature 443:76–80. https://doi.org/10.1038/nature05100

Boudon G, Balcone-Boissard H, Villemant B, Morgan DJ (2015) What factors control superficial lava dome explosivity? Sci Rep 5:14551. https://doi.org/10.1038/srep14551

Braitseva OA, Melekestsev IV, Bogoyavlenskaya GE, Maksimov AP (1991) Bezymianny: eruptive history and dynamics. J Volcanol Seismol 12:165–194

Braitseva OA, Melekestsev I V., Ponomareva V V., Sulerzhitsky LD (1995) Ages of calderas, large explosive craters and active volcanoes in the Kuril-Kamchatka region, Russia. Bull Volcanol 57:383–402. https://doi.org/10.1007/BF00300984

Browne B, Gardner J (2006) The influence of magma ascent path on the texture, mineralogy, and formation of hornblende reaction rims. Earth Planet Sci Lett 246:161–176. https://doi.org/10.1016/j.epsl.2006.05.006

Brugman K, Till CB, Bose M (2022) Common assumptions and methods yield overestimated diffusive timescales, as exemplified in a Yellowstone post-caldera lava. Contrib to Mineral Petrol 177:63. https://doi.org/10.1007/s00410-022-01926-5

Chakraborty S, Dohmen R (2022) Diffusion chronometry of volcanic rocks: looking backward and forward. Bull Volcanol 84:57. https://doi.org/10.1007/s00445-022-01565-5

Chamberlain KJ, Morgan DJ, Wilson CJN (2014) Timescales of mixing and mobilisation in the Bishop Tuff magma body: perspectives from diffusion chronometry. Contrib to Mineral Petrol 168:1034. https://doi.org/10.1007/s00410-014-1034-2

Churikova TG, Dorendorf F, Wörner G (2001) Sources and Fluids in the Mantle Wedge below Kamchatka, Evidence from Across-arc Geochemical Variation. J Petrol 42:1567–1593. https://doi.org/10.1093/petrology/42.8.1567

Cooper GF, Morgan DJ, Wilson CJN (2017) Rapid assembly and rejuvenation of a large silicic magmatic system: Insights from mineral diffusive profiles in the Kidnappers and Rocky Hill deposits, New Zealand. Earth Planet Sci Lett 473:1–13. https://doi.org/10.1016/j.epsl.2017.05.036

Costa F (2021) Clocks in Magmatic Rocks. Annu Rev Earth Planet Sci 49:231–252. https://doi.org/10.1146/annurev-earth-080320-060708

Costa F, Morgan D (2010) Time Constraints from Chemical Equilibration in Magmatic Crystals. John Wiley & Sons, Ltd, Chichester, UK

Costa F, Shea T, Ubide T (2020) Diffusion chronometry and the timescales of magmatic processes. Nat Rev Earth Environ 1:201–214. https://doi.org/10.1038/s43017-020-0038-x

Couch S, Sparks RSJ, Carroll MR (2001) Mineral disequilibrium in lavas explained by convective self-mixing in open magma chambers. Nature 411:1037–1039. https://doi.org/10.1038/35082540

Couperthwaite FK, Thordarson T, Morgan DJ, et al (2020) Diffusion timescales of magmatic processes in the Moinui lava eruption at Mauna Loa, Hawai`i, as inferred from bimodal olivine populations. J Petrol 61:1–19. https://doi.org/10.1093/petrology/egaa058

Criswell CW (1987) Chronology and pyroclastic stratigraphy of the May 18, 1980, Eruption of Mount St. Helens, Washington. J Geophys Res Solid Earth 92:10237–10266. https://doi.org/10.1029/JB092iB10p10237

d'Augustin T (2021) Les éléments halogènes dans les magmas, du traçage des conditions de stockage aux flux éruptifs. PhD thesis, Sorbonne Université

Davydova VO, Shcherbakov VD, Plechov PY, Koulakov IY (2022) Petrological evidence of rapid evolution of the magma plumbing system of Bezymianny volcano in Kamchatka before the December 20th, 2017 eruption. J Volcanol Geotherm Res 421:107422. https://doi.org/10.1016/j.jvolgeores.2021.107422

Davydova VO, Shcherbakov VD, Plechov PY, Perepelov AB (2017) Petrology of mafic enclaves in the 2006–2012 eruptive products of Bezymianny Volcano, Kamchatka. Petrology 25:592–614. https://doi.org/10.1134/S0869591117060029

DeMets C (1992) Oblique convergence and deformation along the Kuril and Japan Trenches. J Geophys Res 97:17615. https://doi.org/10.1029/92JB01306

Devine JD, Rutherford MJ, Norton GE, Young SR (2003) Magma Storage Region Processes Inferred from Geochemistry of Fe-Ti Oxides in Andesitic Magma, Soufriere Hills Volcano, Montserrat, W.I. J Petrol 44:1375–1400. https://doi.org/10.1093/petrology/44.8.1375

Druitt TH, Costa F, Deloule E, et al (2012) Decadal to monthly timescales of magma transfer and reservoir growth at a caldera volcano. Nature 482:77–80. https://doi.org/10.1038/nature10706

Endo E, Malone SD, Noson LS, Weaver CS (1981) Locations, magnitudes and statistics of the March 20-May 18 earthquake sequence. US Geol ogical Surv Prof Pap 1250:93–107

Ewert JW, Diefenbach AK, Ramsey DW (2018) 2018 update to the U.S. Geological Survey national volcanic threat assessment: U.S. Geological Survey Scientific Investigations Report 2018–5140

Fabbro GN, Druitt TH, Costa F (2018) Storage and Eruption of Silicic Magma across the Transition from Dominantly Effusive to Caldera-forming States at an Arc Volcano (Santorini, Greece). J Petrol 58:2429–2464. https://doi.org/10.1093/petrology/egy013

Fedotov SA, Zharinov NA, Gontovaya LI (2010) The magmatic system of the Klyuchevskaya group of volcanoes inferred from data on its eruptions, earthquakes, deformation, and deep structure. J Volcanol Seismol 4:1–33. https://doi.org/10.1134/S074204631001001X

Fick A (1855) V. On liquid diffusion. London, Edinburgh, Dublin Philos Mag J Sci 10:30–39. https://doi.org/10.1080/14786445508641925

Flaherty T, Druitt TH, Tuffen H, et al (2018) Multiple timescale constraints for high-flux magma chamber assembly prior to the Late Bronze Age eruption of Santorini (Greece). Contrib to Mineral Petrol 173:75. https://doi.org/10.1007/s00410-018-1490-1

Frey HM, Lange RA (2011) Phenocryst complexity in andesites and dacites from the Tequila volcanic field, Mexico: resolving the effects of degassing vs. magma mixing. Contrib to Mineral Petrol 162:415–445. https://doi.org/10.1007/s00410-010-0604-1

Gaillard F, Scaillet B (2014) A theoretical framework for volcanic degassing chemistry in a comparative planetology perspective and implications for planetary atmospheres. Earth Planet Sci Lett 403:307–316. https://doi.org/10.1016/j.epsl.2014.07.009

Ganguly J, Tazzoli V (1994) Fe2+-Mg interdiffusion in orthopyroxene: retrieval from the data on intracrystalline exchange reaction. Am Mineral 79:930–937

Giacomoni PP, Ferlito C, Coltorti M, et al (2014) Plagioclase as archive of magma ascent dynamics on “open conduit” volcanoes: The 2001–2006 eruptive period at Mt. Etna. Earth-Science Rev 138:371–393. https://doi.org/10.1016/j.earscirev.2014.06.009

Girina OA (2013) Chronology of Bezymianny Volcano activity, 1956–2010. J Volcanol Geotherm Res 263:22–41. https://doi.org/10.1016/j.jvolgeores.2013.05.002

Glicken H (1998) Rockslide-debris avalanche of May 18, 1980, Mount St. Helens Volcano, Washington

Global Volcanism Program (2023) Bezymianny. In: Glob. Volcanism Progr. · Dep. Miner. Sci. · Natl. Museum Nat. Hist. Smithson. Inst. https://volcano.si.edu/volcano.cfm?vn=300250#bgvn_201706. Accessed 28 Aug 2022

Gorshkov GS (1959) Gigantic eruption of the volcano bezymianny. Bull Volcanol 20:77–109. https://doi.org/10.1007/BF02596572

Gorshkov GS, Bogoyavlenskaya GE (1965) Bezymianny Volcano and Peculiarities of Its Last Eruptions in 1955–1963. 172

Hawkesworth C, George R, Turner S, Zellmer G (2004) Time scales of magmatic processes. Earth Planet Sci Lett 218:1–16. https://doi.org/10.1016/S0012-821X(03)00634-4

Higgins O, Sheldrake T, Caricchi L (2022) Machine learning thermobarometry and chemometry using amphibole and clinopyroxene: a window into the roots of an arc volcano (Mount Liamuiga, Saint Kitts). Contrib to Mineral Petrol 177:10. https://doi.org/10.1007/s00410-021-01874-6

Journeau C, Shapiro NM, Seydoux L, et al (2022) Seismic tremor reveals active trans-crustal magmatic system beneath Kamchatka volcanoes. Sci Adv 8:. https://doi.org/10.1126/sciadv.abj1571

Jugo PJ (2009) Sulfur content at sulfide saturation in oxidized magmas. Geology 37:415–418. https://doi.org/10.1130/G25527A.1

Kahl M, Chakraborty S, Costa F, et al (2013) Compositionally zoned crystals and real-time degassing data reveal changes in magma transfer dynamics during the 2006 summit eruptive episodes of Mt. Etna. Bull Volcanol 75:692. https://doi.org/10.1007/s00445-013-0692-7

Kahl M, Chakraborty S, Costa F, Pompilio M (2011) Dynamic plumbing system beneath volcanoes revealed by kinetic modeling, and the connection to monitoring data: An example from Mt. Etna. Earth Planet Sci Lett 308:11–22. https://doi.org/10.1016/j.epsl.2011.05.008

Kahl M, Mutch EJF, Maclennan J, et al (2023) Deep magma mobilization years before the 2021 CE Fagradalsfjall eruption, Iceland. Geology 51:184–188. https://doi.org/10.1130/G50340.1

Kilgour GN, Saunders KE, Blundy JD, et al (2014) Timescales of magmatic processes at Ruapehu volcano from diffusion chronometry and their comparison to monitoring data. J Volcanol Geotherm Res 288:62–75. https://doi.org/10.1016/j.jvolgeores.2014.09.010

Koulakov I, Abkadyrov I, Al Arifi N, et al (2017) Three different types of plumbing system beneath the neighboring active volcanoes of Tolbachik, Bezymianny, and Klyuchevskoy in Kamchatka. J Geophys Res Solid Earth 122:3852–3874. https://doi.org/10.1002/2017JB014082

Koulakov I, Gordeev EI, Dobretsov NL, et al (2013) Rapid changes in magma storage beneath the Klyuchevskoy group of volcanoes inferred from time-dependent seismic tomography. J Volcanol Geotherm Res 263:75–91. https://doi.org/10.1016/j.jvolgeores.2012.10.014

Koulakov I, Plechov P, Mania R, et al (2021) Anatomy of the Bezymianny volcano merely before an explosive eruption on 20.12.2017. Sci Rep 11:1758. https://doi.org/10.1038/s41598-021-81498-9

Koulakov I, Shapiro NM, Sens-Schönfelder C, et al (2020) Mantle and Crustal Sources of Magmatic Activity of Klyuchevskoy and Surrounding Volcanoes in Kamchatka Inferred From Earthquake Tomography. J Geophys Res Solid Earth 125:1–29. https://doi.org/10.1029/2020JB020097

Levin V, Shapiro N, Park J, Ritzwoller M (2002) Seismic evidence for catastrophic slab loss beneath Kamchatka. Nature 418:763–767. https://doi.org/10.1038/nature00973

Lipman PW, Mullineaux DR (1981) The 1980 eruptions of Mount St. Helens, Washington

Magee R, Ubide T, Kahl M (2020) The Lead-up to Mount Etna's Most Destructive Historic Eruption (1669). Cryptic Recharge Recorded in Clinopyroxene. J Petrol 61:. https://doi.org/10.1093/petrology/egaa025

Mania R, Walter TR, Belousova M, et al (2019) Deformations and Morphology Changes Associated with the 2016–2017 Eruption Sequence at Bezymianny Volcano, Kamchatka. Remote Sens 11:1278. https://doi.org/10.3390/rs11111278

Martel C, Erdmann S, Boudon G, et al The 1956 eruption of Bezymianny volcano (Kamchatka). Part I - Petrological constraints on magma storage and eruptive dynamics. accepted

Martel C, Pichavant M, Holtz F, et al (1999) Effects of fO2 and H2O on andesite phase relations between 2 and 4 kbar. J Geophys Res Solid Earth 104:29453–29470. https://doi.org/10.1029/1999JB900191

Melekestsev I V., Ponomareva V V., Volynets ON (1995) Kizimen volcano, Kamchatka — A future Mount St. Helens? J Volcanol Geotherm Res 65:205–226. https://doi.org/10.1016/0377-0273(94)00082-R

Melnik O, Lyakhovsky V, Shapiro NM, et al (2020) Deep long period volcanic earthquakes generated by degassing of volatile-rich basaltic magmas. Nat Commun 11:3918. https://doi.org/10.1038/s41467-020-17759-4

Metcalfe A, Moune S, Komorowski J-C, et al (2021) Magmatic Processes at La Soufrière de Guadeloupe: Insights From Crystal Studies and Diffusion Timescales for Eruption Onset. Front Earth Sci 9:1–28. https://doi.org/10.3389/feart.2021.617294

Ostorero L, Balcone-Boissard H, Boudon G, et al (2022) Correlated petrology and seismicity indicate rapid magma accumulation prior to eruption of Kizimen volcano, Kamchatka. Commun Earth Environ 3:290. https://doi.org/10.1038/s43247-022-00622-3

Ostorero L, Boudon G, Boissard HB, et al (2021) Time - window into the transcrustal plumbing system dynamics of Dominica (Lesser Antilles). Sci Rep 11:1–15. https://doi.org/10.1038/s41598-021-90831-1

Petrelli M (2021) Introduction to Python in Earth Science Data Analysis. Springer International Publishing, Cham

Petrone CM, Braschi E, Francalanci L, et al (2018) Rapid mixing and short storage timescale in the magma dynamics of a steady-state volcano. Earth Planet Sci Lett 492:206–221. https://doi.org/10.1016/j.epsl.2018.03.055

Petrone CM, Bugatti G, Braschi E, Tommasini S (2016) Pre-eruptive magmatic processes re-timed using a non-isothermal approach to magma chamber dynamics. Nat Commun 7:12946. https://doi.org/10.1038/ncomms12946

Petrone CM, Mangler MF (2021) Elemental Diffusion Chronostratigraphy. In: Masotta M, Beier C, Mollo S (eds) Crustal Magmatic System Evolution. Wiley, pp 177–193

Plechov PY, Tsai AE, Shcherbakov VD, Dirksen O V. (2008) Opacitization conditions of hornblende in Bezymyannyi volcano andesites (March 30, 1956 eruption). Petrology 16:19–35. https://doi.org/10.1134/S0869591108010025

Putirka KD (2008) Thermometers and Barometers for Volcanic Systems. Rev Mineral Geochemistry 69:61–120. https://doi.org/10.2138/rmg.2008.69.3

Rout SS, Schmidt BC, Wörner G (2020) Constraints on non-isothermal diffusion modeling: An experimental analysis and error assessment using halogen diffusion in melts. Am Mineral 105:227–238. https://doi.org/10.2138/am-2020-7193

Rutherford MJ, Devine JD (2003) Magmatic Conditions and Magma Ascent as Indicated by Hornblende Phase Equilibria and Reactions in the 1995-2002 Soufriere Hills Magma. J Petrol 44:1433–1453. https://doi.org/10.1093/petrology/44.8.1433

Rutherford MJ, Hill PM (1993) Magma ascent rates from amphibole breakdown: An experimental study applied to the 1980-1986 Mount St. Helens eruptions. J Geophys Res Solid Earth 98:19667–19685. https://doi.org/10.1029/93JB01613

Saunders K, Blundy J, Dohmen R, Cashman K (2012) Linking Petrology and Seismology at an Active Volcano. Science (80-) 336:1023–1027. https://doi.org/10.1126/science.1220066

Scandone R, Cashman K V., Malone SD (2007) Magma supply, magma ascent and the style of volcanic eruptions. Earth Planet Sci Lett 253:513–529. https://doi.org/10.1016/j.epsl.2006.11.016

Shamloo HI, Till CB (2019) Decadal transition from quiescence to supereruption: petrologic investigation of the Lava Creek Tuff, Yellowstone Caldera, WY. Contrib to Mineral Petrol 174:32. https://doi.org/10.1007/s00410-019-1570-x

Shapiro NM, Droznin D V., Droznina SY, et al (2017) Deep and shallow long-period volcanic seismicity linked by fluid-pressure transfer. Nat Geosci 10:442–445. https://doi.org/10.1038/ngeo2952

Shcherbakov VD, Neill OK, Izbekov PE, Plechov PY (2013) Phase equilibria constraints on pre-eruptive magma storage conditions for the 1956 eruption of Bezymianny Volcano, Kamchatka, Russia. J Volcanol Geotherm Res 263:132–140. https://doi.org/10.1016/j.jvolgeores.2013.02.010

Singer BS, Costa F, Herrin JS, et al (2016) The timing of compositionally-zoned magma reservoirs and mafic ‘priming’ weeks before the 1912 Novarupta-Katmai rhyolite eruption. Earth Planet Sci Lett 451:125–137. https://doi.org/10.1016/j.epsl.2016.07.015

Solaro C, Balcone-Boissard H, Morgan DJ, et al (2020) A System Dynamics Approach to Understanding the deep Magma Plumbing System Beneath Dominica (Lesser Antilles). Front Earth Sci 8:. https://doi.org/10.3389/feart.2020.574032

Streck MJ (2008) Mineral Textures and Zoning as Evidence for Open System Processes. Rev Mineral Geochemistry 69:595–622. https://doi.org/10.2138/rmg.2008.69.15

Thelen W, West M, Senyukov S (2010) Seismic characterization of the fall 2007 eruptive sequence at Bezymianny Volcano, Russia. J Volcanol Geotherm Res 194:201–213. https://doi.org/10.1016/j.jvolgeores.2010.05.010

Tokarev PI (1985) The prediction of large explosions of andesitic volcanoes. J Geodyn 3:219–244. https://doi.org/10.1016/0264-3707(85)90036-5

Tokarev PI (1981) Volcanic Earthquakes of Kamchatka. Nauka, Moscow, Russia, p 164

Turner SJ, Izbekov P, Langmuir C (2013) The magma plumbing system of Bezymianny Volcano: Insights from a 54year time series of trace element whole-rock geochemistry and amphibole compositions. J Volcanol Geotherm Res 263:108–121. https://doi.org/10.1016/j.jvolgeores.2012.12.014

Voight B (1981) Time scale for the first movements of the May 18 eruption. In: Lipman PW, Mullineaux DR (eds) The 1980 eruptions of Mount St. Helens, US Geol Su. Washington, pp 69–86

Voight B, Glicken H, Janda RJ, Douglass PM (1981) Catastrophic rockslide avalanche of May 18. In: Lipman PW, Mullineaux DR (eds) The 1980 eruptions of Mount St. Helens, US Geol Su. Washington, pp 347–377

Figure and table caption

Fig. 1 Bezymianny volcano in Kamchatka (summit location marked with a triangle). a) Kamchatka map with the three volcanic zones: Sredinny Range (SR), Central Kamchatka Depression (CKD) and Eastern Volcanic Front (EVF) (Melekestsev et al. 1995; Churikova et al. 2001). Image credit: Nasa Earth Observatory shaded and colored Shuttle Radar Topography Mission (SRTM) elevation model from February 2000, image courtesy of the SRTM Team NASA/JPL/NIMA. The inset shows the location of Kamchatka on the globe (credit: Google Earth V 7.3.4.8642; July, 2022. Kamchatka, 56° 7.951'N, 159° 31.844'E, view from space, altitude 14,905 km. Image Landsat/Copernicus. Data SIO, NOAA, U.S. Navy, NGA, GEBCO. Image IBCAO. [10 July 10 2022]). b) Bezymianny, with the boundary of the debris avalanche deposit and the laterally directed blast deposits from 30 March 1956 flank collapse, located below the new deposits from eruptions that followed (Belousov 1996) and sampling sites (**Supplementary Table 1; Supplementary Fig. 1**). The white dashed line shows the scar of Bezymianny's flank collapse in 1956. Image credit: Google Earth V 7.3.4.8248 (July, 2013). Bezymianny, Kamchatka, 55° 56.880'N, 160° 40.282'E, eye altitude 17.57 km. Image Landsat/Copernicus. Maxar Technologies 2022. [April 12, 2021]

Fig. 2 Timeline of the preclimactic, climactic as well as post-eruptive phases of Bezymianny 1955-1956 (all pictures are from Gorshkov (1959)). The pre-eruptive stage consisted of a seismic swarm recorded from 29 September 1955 to 22 October 1955. Some seismicity may have been generated before, as the only seismic station present was located 42 km away from the volcano (Tokarev 1981, 1985; Belousov and Belousova 1998). On 22 October, the preclimactic phase began, with phreatic to phreatomagmatic explosions (a) until the end of November 1955. a) Picture of Bezymianny on 30 October 1955. b) Fumarolic activity observed on 25 January 1956 during the overflight of Bezymianny. Deformation of the SE flank and uplift of the old dome was observed; comparison of earlier pictures with those taken in February revealed an uplift of 100 m (Gorshkov 1959); (c) Bezymianny in July 1949, with the black dashed line showing the outline of the volcano in February 1956 and red dots, indicating the crater in October 1955; d) On 30 March 1956, a large volcanic earthquake due to intruding magma triggered a large-sector collapse, generating a debris avalanche (Belousov and Belousova 1998). The collapse unroofed the cryptodome, resulting in a directed lateral blast due to rapid decompression (view from Kozyresk village), leaving a horseshoe-shape topography (1.7 x 2.8 km) (Belousov et al. 2007). The blast was immediately followed by post-blast pumiceous C-PDC and an ash cloud of 34-38 km high was jointly produced by the blast and post-blast PDC. e) Picture of Bezymianny after the 1956 eruption, with the black line showing the outline of the volcano before the eruption. The amphitheater scar is outlined in orange. f) Lava dome growth then constituted the post-climactic stage, that continues until now

Fig. 3 Back-scattered electron (BSE) images of the zoning types identified in the orthopyroxene crystals of Bezymianny 1956. a) Unzoned orthopyroxene; b-c) Two types of single-zoned orthopyroxene: normal-zoned (b), with a Mg-rich core (darker zone on a grayscale image) and Fe-rich rims (clearer in grayscale), or reverse-zoned (c), with a Fe-rich core and Mg-rich rims; (d-i) Multiple-zoned orthopyroxene crystals, either normal + reverse (d) or reverse + normal (e) or with three bands (normal + reverse + normal (f), or reverse + normal + reverse bands (g)) to four (h) or more than five bands (i). Schemes of the different zoning types are shown in Supplementary Fig. 6. The white areas are magnetite crystals or melt inclusions. j) BSE image of multiple-zoned and unzoned orthopyroxene crystals with the corresponding chemical map displaying Mg (in blue) in (k)

Fig. 4 Proportions of the zonations identified in the orthopyroxene crystals of: (a) the blast in all size fractions (500-710, 315-500, 250-355 and 125-250 µm) and (b) the post-blast pumiceous C-PDC, in the size fractions between 315-500, 250-355 and 125-250 µm. The major zonations are highlighted in grey. The detailed proportions of zonations in each fraction are shown in Supplementary Fig. 7. NZ: normal-zoned orthopyroxene, RZ: reverse-zoned and MZ: multiple-zoned. The percentage of the multiple-zoned population recording normal zoning surrounded by reverse zoning are specified

Fig. 5 En contents of the zoned and unzoned orthopyroxene crystals (opx) of the blast and post-blast pumiceous C-PDC. Probability density functions (PDF) of the En content of unzoned (a-b) and zoned orthopyroxene crystals (cores (c and e) and all bands (d and f). Gaussian Kernel Density Estimation (KDE) was used to estimate the probability density functions of the En content of the orthopyroxene crystals adapting the code of Petrelli (2021). g-h) External reverse and normal rims (N) are shown, as are the compositions of the bands before (N-1) and their zoning types compared to the N-2 band (either normal or reverse). Single-zoned rims are also shown for orthopyroxene crystals of the post-blast C-PDC pumices (dark dashed histograms). Two main En contents can be identified, with rims evolving either toward En-richer or En-poorer contents (c-g), separating the En content of the orthopyroxene between En_{58-65} and En_{65-68}. n is the number of orthopyroxene (opx) crystals analyzed

Fig. 6 Compositions of magnetite crystals (a-b) and probability density curves of the timescales modelled in the blast and post-blast C-PDC pumices (c-d). a-b) TiO_2 vs FeO compositions of the zoned magnetite crystals for the blast and post-blast pumiceous C-PDC (for cores and rims); c) Probability density function of the timescales modelled in the reverse-zoned magnetite crystals with the temperature of 900 ± 50 °C estimated by Martel et al. (accepted) for the shallow storage, considering the uncertainties associated to the individual timescales. These uncertainties on individual timescale calculations are shown in **Supplementary Fig. 13** and **Supplementary Data 7**. n in (a-b) is the number of magnetite crystals investigated and n in (c) is the number of timescales modelled

Fig. 7 Examples of best-fit models obtained after intercalibration of EMP compositional profiles and BSE grey level data of profiles in multiple-zoned orthopyroxene crystals ("B" for bands) for a temperature of 900 °C (Supplementary Table 6). a) Normal-zoned profile; b-d) Reverse-zoned profiles. Dashed lines show the initial step model used to model the diffusion timescales. Uncertainties associated to the timescales are calculated using a Monte Carlo simulation (Supplementary Data 3). Standard deviation on the Mg# is shown. More details in the Supplementary Materials and Supplementary Figure 3 can be found.

Fig. 8 Probability density functions of the Fe-Mg interdiffusion timescales for orthopyroxene crystals considering the uncertainties associated to the individual timescales. The timescales are modelled on the major compositional changes evidenced in orthopyroxene crystals depending on the location of the rim modelled in the blast (a) and post-blast C-PDC pumices (b) (normal zoning, from En_{65-68} to En_{58-64}) and then, reverse zoning, from En_{59-64} to En_{65-68}, for the inner rims, or N-1 bands or external rims N (**Fig. 5; Supplementary Data 6**). c-d) Focus on the 500 days period prior to the climactic phase of the eruption. The timescales were modelled using the temperature of 900 ± 50 °C estimated by Martel et al. (accepted) for the shallow storage and 850 ± 50 °C for the core to inner normal bands. The uncertainties of the individual timescales calculations are shown in **Supplementary Fig. 12-13** and **Supplementary Data 6**. For the blast and the core-inner normal zoned band, the PDF could not be made as only one timescale was modelled on a core to inner band in a multiple-zoned crystal. n is the number of timescales modelled and N is the location of the rim. "yr" and "m" are the abbreviations of "years" and "months", respectively

Fig. 9 Timescale constraints for the formation of amphibole decompression rims at low and very low pressures. a) Summary of decomposition rim growth rates (G) for single-step decompression experiments. Data from Rutherford & Hill (1993) for decompression experiments for 900 °C and 20 or 90 MPa (yellow symbols) and 860 °C and 90 MPa (blue symbols) and data from Browne & Gardner (2006) for 840 °C and 10 to 95 MPa. Decomposition rim growth rate decreases with decomposition pressure and temperature (as shown) and also with time (not shown). The conditions of the single-step experiments with equilibration at 90 MPa and 840-900 °C closely correspond to those estimated for amphibole decomposition in Bezymianny's system (< 100 to < 25 MPa and > 850 to ~950 °C). The experimental constraints can thus be used as constraints for the natural system, but possible small differences in temperature (e.g. possibly as high as ~950 °C in the natural system) cannot be quantified and the estimated timescales remain necessarily broad. The outlined fields mark the range of inferred equilibration pressures and probable range of decomposition rates inferred from the Rutherford & Hill (1993) and Browne & Gardner (2006) experimental data for Type-1 rims (red box), intermediate type rims (pink box), and Type-2 rims (blue box). b) Inferred shallow and very shallow amphibole residence times below the amphibole stability field for Type-1, intermediate type, and Type-2 rims for the whole range of rim growth rates ("broad estimate" in text and **Supplementary Table 4**) and for the inferred likely rim growth rates ("best estimate" in text and **Supplementary Table 4**). c-d) Probability density functions of the amphibole timescales considering the uncertainties associated to the individual timescales using (c) the higher likely growth rate or (d) the lower likely growth rate for the blast clasts and C-PDC pumices. The uncertainties on individual timescale calculations are shown in **Supplementary Fig. 13** and **Supplementary Table 4**. n in (b-d) is the number of amphibole crystals investigated

Fig. 10 Magma dynamics inferred for the 1956 climactic phase of Bezymianny from the combined point of view of orthopyroxene, magnetite and amphibole crystals in this study (Fig. 6-9), with the architecture of the magma plumbing system from Martel et al. (accepted). Geophysical observations are from Gorshkov (1959), Gorshkov and Bogoyavlenskaya (1965) and Belousov and Belousova (1998). a) Using orthopyroxene textures and timescales, we infer that self-mixing occurred in the deep reservoir several years before the climactic phase of the eruption (from reverse and normal zoning of inner bands of orthopyroxene crystals). b) Then, from 2 years to 6 months before the climactic phase, degassing of the magma occurred and formed normal zonings in orthopyroxene and recorded by melt inclusions hosted in orthopyroxene. c) Six months before, several minor orthopyroxene reverse zonings recorded self-mixing in the reservoir. d) From 3 to 2 months before, magma ascent began to occur to form the shallow reservoir. Heating from a magma injection in the deep reservoir (Martel et al. accepted) or degassing driven crystallization with possible oxidation generated external reverse-zoned rims of orthopyroxene and magnetite and Type-2 amphibole. This mafic melt injection could have generated overpressure and favored magma ascent to the shallow reservoir (Martel et al. accepted). At the same time, the blast magma migrated to the very shallow zone forming a cryptodome (< 25 MPa) (generated from external normal-zoned orthopyroxene crystals, intermediate type amphibole and the presence of cristobalite). Normal-zoned orthopyroxene crystals from C-PDC pumices also show the beginning of magma ascent around the same time into the shallow storage zone. e) Finally, magma at the origin of the post-blast C-PDC pumices ascended in the shallow area a few days before the eruption, generating Type-1 amphibole and other amphibole crystals from the C-PDC pumices (Shcherbakov et al. 2013). f) The paroxysmal eruption of Bezymianny then occurred, on 30 March 1956, following the collapse of part of the flank of Bezymianny. Dashed outlined lenses can correspond to old, almost cooled reservoirs. "opx" stands for orthopyroxene, "mgt" for magnetite, "plag" for plagioclase and "amph" for amphibole crystals

All figures

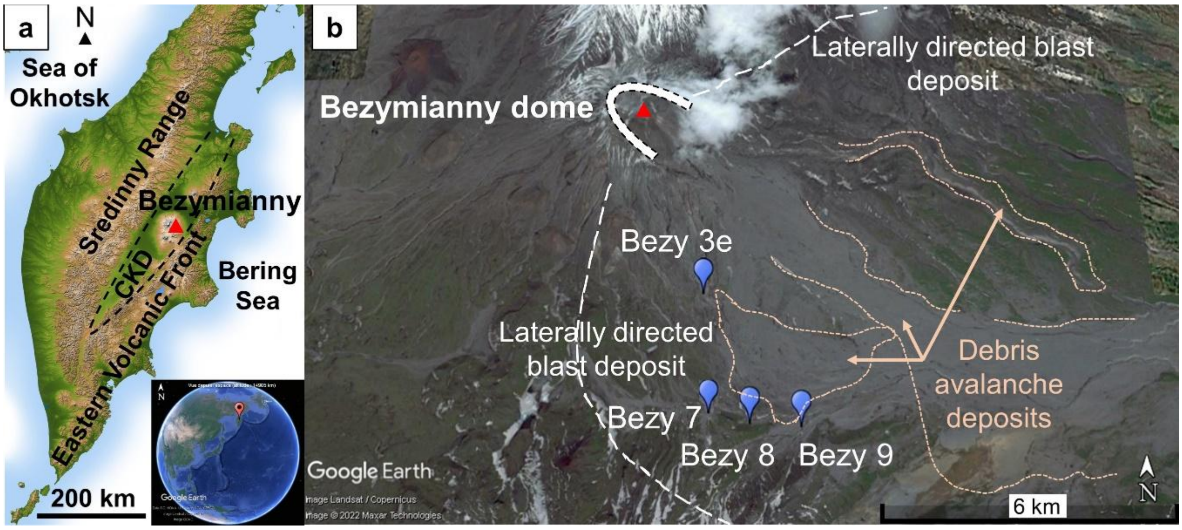

Fig. 1 Bezymianny volcano in Kamchatka (summit location marked with a triangle). a) Kamchatka map with the three volcanic zones: Sredinny Range (SR), Central Kamchatka Depression (CKD) and Eastern Volcanic Front (EVF) (Melekestsev et al. 1995; Churikova et al. 2001). Image credit: Nasa Earth Observatory shaded and colored Shuttle Radar Topography Mission (SRTM) elevation model from February 2000, image courtesy of the SRTM Team NASA/JPL/NIMA. The inset shows the location of Kamchatka on the globe (credit: Google Earth V 7.3.4.8642; July, 2022. Kamchatka, 56° 7.951'N, 159° 31.844'E, view from space, altitude 14,905 km. Image Landsat/Copernicus. Data SIO, NOAA, U.S. Navy, NGA, GEBCO. Image IBCAO. [10 July 10 2022]). b) Bezymianny, with the boundary of the debris avalanche deposit and the laterally directed blast deposits from 30 March 1956 flank collapse, located below the new deposits from eruptions that followed (Belousov 1996) and sampling sites (**Supplementary Table 1; Supplementary Fig. 1**). The white dashed line shows the scar of Bezymianny's flank collapse in 1956. Image credit: Google Earth V 7.3.4.8248 (July, 2013). Bezymianny, Kamchatka, 55° 56.880'N, 160° 40.282'E, eye altitude 17.57 km. Image Landsat/Copernicus. Maxar Technologies 2022. [April 12, 2021]

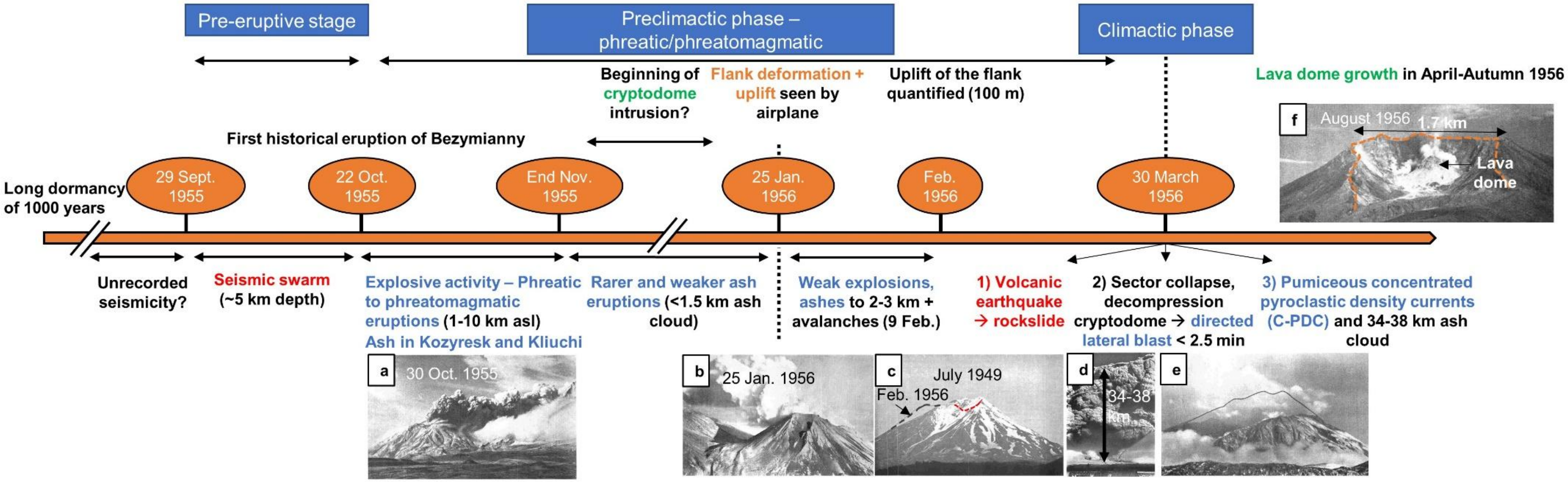

Fig. 2 Timeline of the preclimactic, climactic as well as post-eruptive phases of Bezymianny 1955-1956 (all pictures are from Gorshkov (1959)). The pre-eruptive stage consisted of a seismic swarm recorded from 29 September 1955 to 22 October 1955. Some seismicity may have been generated before, as the only seismic station present was located 42 km away from the volcano (Tokarev 1981, 1985; Belousov and Belousova 1998). On 22 October, the preclimactic phase began, with phreatic to phreatomagmatic explosions (a) until the end of November 1955. a) Picture of Bezymianny on 30 October 1955. b) Fumarolic activity observed on 25 January 1956 during the overflight of Bezymianny. Deformation of the SE flank and uplift of the old dome was observed; comparison of earlier pictures with those taken in February revealed an uplift of 100 m (Gorshkov 1959); (c) Bezymianny in July 1949, with the black dashed line showing the outline of the volcano in February 1956 and red dots, indicating the crater in October 1955; d) On 30 March 1956, a large volcanic earthquake due to intruding magma triggered a large-sector collapse, generating a debris avalanche (Belousov and Belousova 1998). The collapse unroofed the cryptodome, resulting in a directed lateral blast due to rapid decompression (view from Kozyresk village), leaving a horseshoe-shape topography (1.7 x 2.8 km) (Belousov et al. 2007). The blast was immediately followed by post-blast pumiceous C-PDC and an ash cloud of 34-38 km high was jointly produced by the blast and post-blast PDC. e) Picture of Bezymianny after the 1956 eruption, with the black line showing the outline of the volcano before the eruption. The amphitheater scar is outlined in orange. f) Lava dome growth then constituted the post-climactic stage, that continues until now

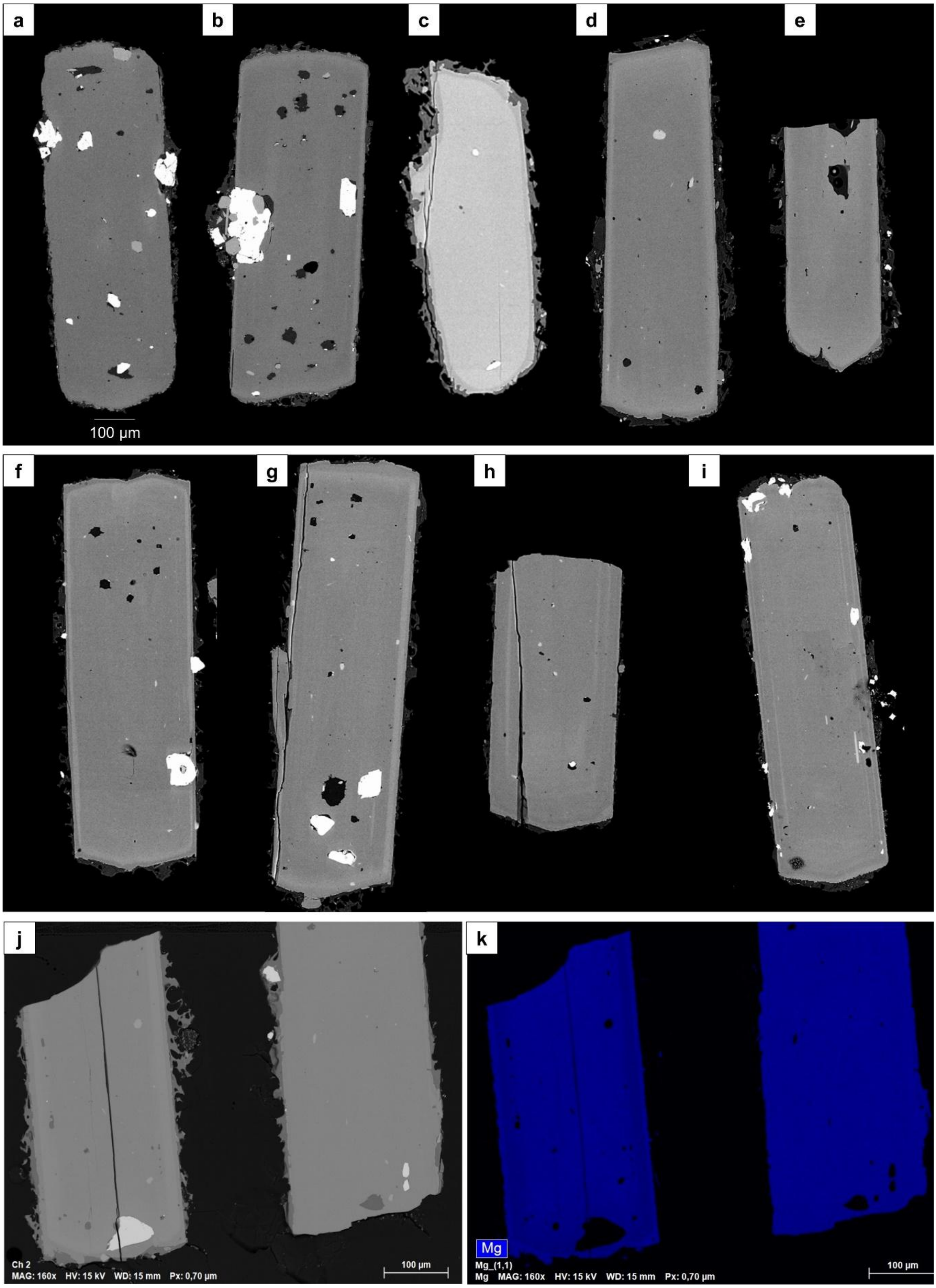

Fig. 3 Back-scattered electron (BSE) images of the zoning types identified in the orthopyroxene crystals of Bezymianny 1956. a) Unzoned orthopyroxene; b-c) Two types of single-zoned orthopyroxene: normal-zoned (b), with a Mg-rich core (darker zone on a grayscale image) and Fe-rich rims (clearer in grayscale), or reverse-zoned (c), with a Fe-rich core and Mg-rich rims; (d-i) Multiple-zoned orthopyroxene crystals, either normal + reverse (d) or reverse + normal (e) or with three bands

(normal + reverse + normal (f), or reverse + normal + reverse bands (g)) to four (h) or more than five bands (i). Schemes of the different zoning types are shown in Supplementary Fig. 6. The white areas are magnetite crystals or melt inclusions. j) BSE image of multiple-zoned and unzoned orthopyroxene crystals with the corresponding chemical map displaying Mg (in blue) in (k)

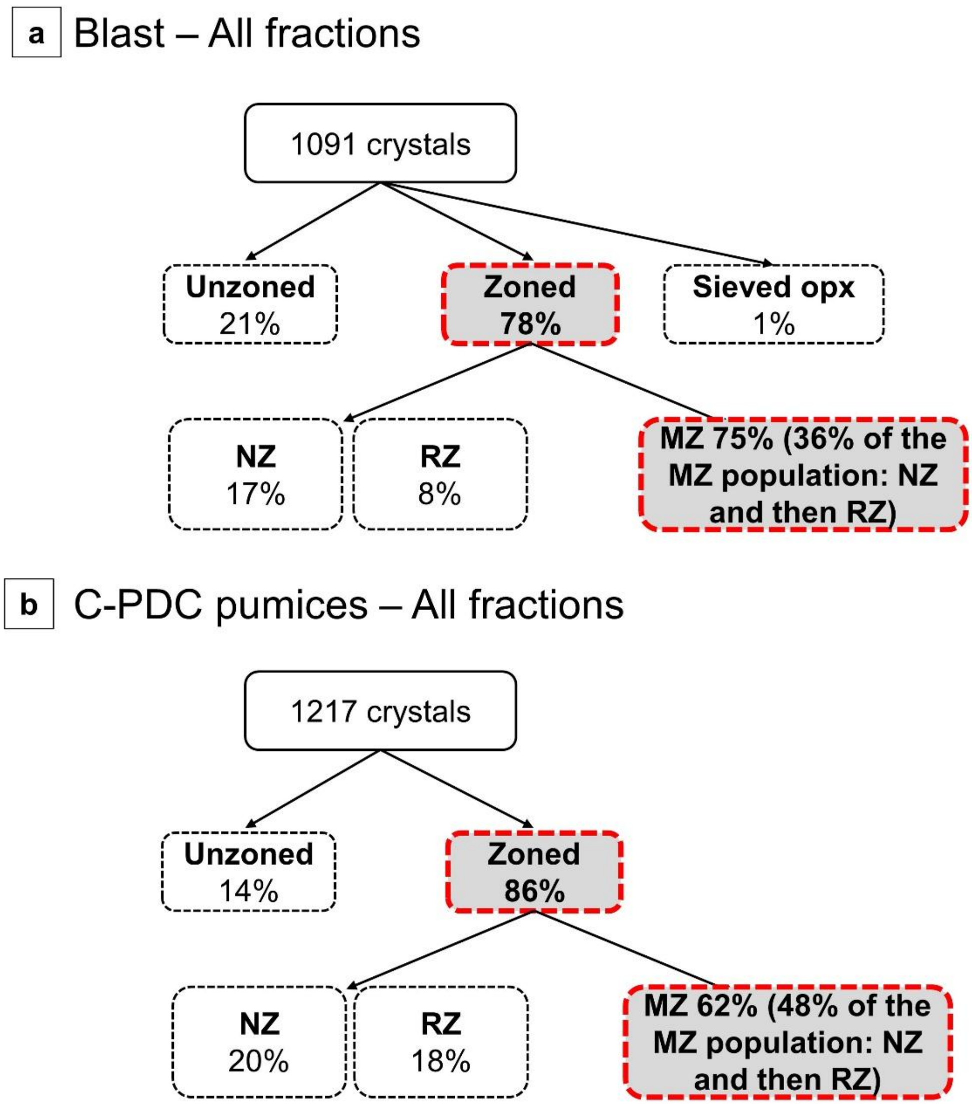

Fig. 4 Proportions of the zonations identified in the orthopyroxene crystals of: (a) the blast in all size fractions (500-710, 315-500, 250-355 and 125-250 µm) and (b) the post-blast pumiceous C-PDC, in the size fractions between 315-500, 250-355 and 125-250 µm. The major zonations are highlighted in grey. The detailed proportions of zonations in each fraction are shown in Supplementary Fig. 7. NZ: normal-zoned orthopyroxene, RZ: reverse-zoned and MZ: multiple-zoned. The percentage of the multiple-zoned population recording normal zoning surrounded by reverse zoning are specified

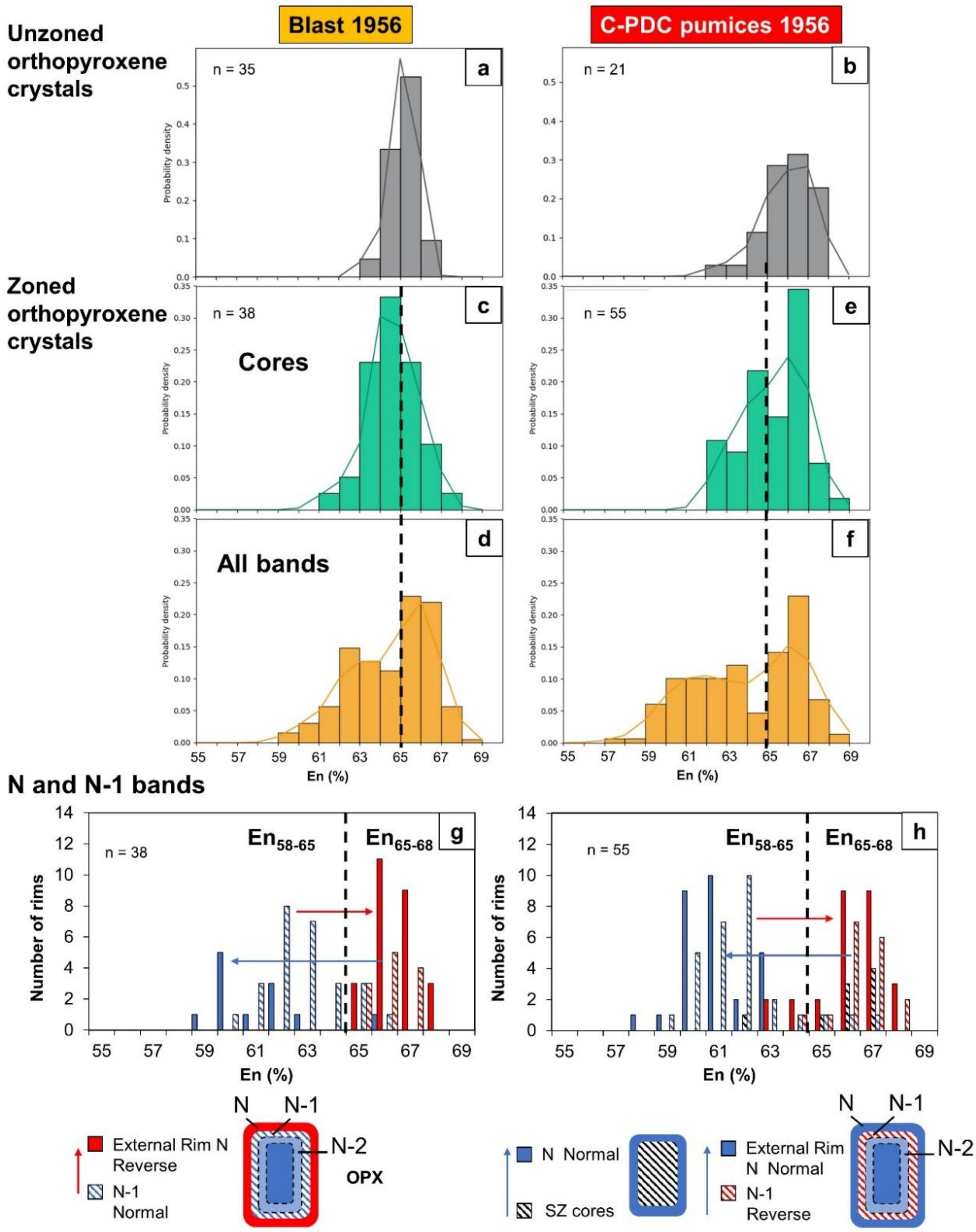

Fig. 5 En contents of the zoned and unzoned orthopyroxene crystals (opx) of the blast and post-blast pumiceous C-PDC. Probability density functions (PDF) of the En content of unzoned (a-b) and zoned orthopyroxene crystals (cores (c and e) and all bands (d and f). Gaussian Kernel Density Estimation (KDE) was used to estimate the probability density functions of the En content of the orthopyroxene crystals adapting the code of Petrelli (2021). g-h) External reverse and normal rims (N) are shown, as are the compositions of the bands before (N-1) and their zoning types compared to the N-2 band (either normal or reverse). Single-zoned rims are also shown for orthopyroxene crystals of the post-blast C-PDC pumices (dark dashed histograms). Two main En contents can be identified, with rims evolving either toward En-richer or En-poorer contents (c-g), separating the En content of the orthopyroxene between En_{58-65} and En_{65-68}. n is the number of orthopyroxene (opx) crystals analyzed

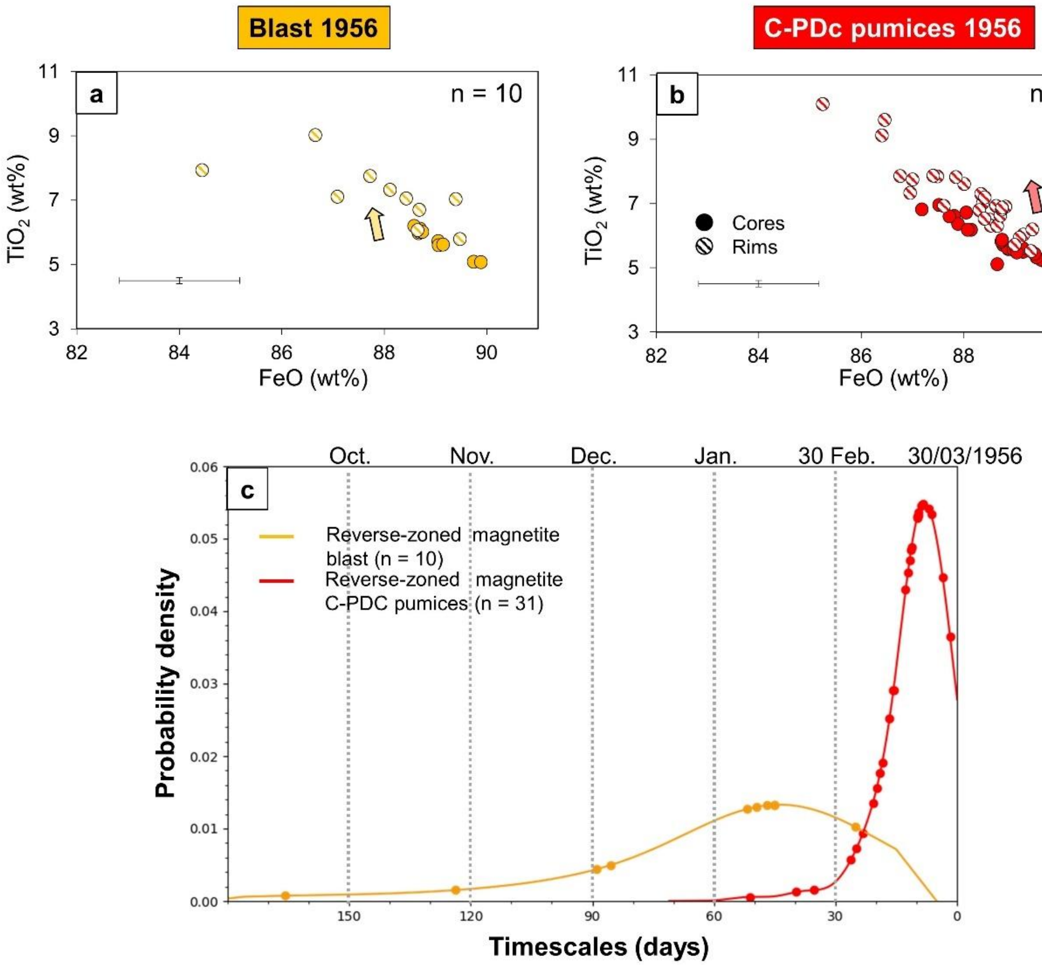

Fig. 6 Compositions of magnetite crystals (a-b) and probability density curves of the timescales modelled in the blast and post-blast C-PDC pumices (c). a-b) TiO_2 vs FeO compositions of the zoned magnetite crystals for the blast and post-blast pumiceous C-PDC (for cores and rims); c) Probability density function of the timescales modelled in the reverse-zoned magnetite crystals with the temperature of 900 ± 50 °C estimated by Martel et al. (accepted) for the shallow storage, considering the uncertainties associated to the individual timescales. These uncertainties on individual timescale calculations are shown in **Supplementary Fig. 13** and **Supplementary Data 7**. n in (a-b) is the number of magnetite crystals investigated and n in (c) is the number of timescales modelled

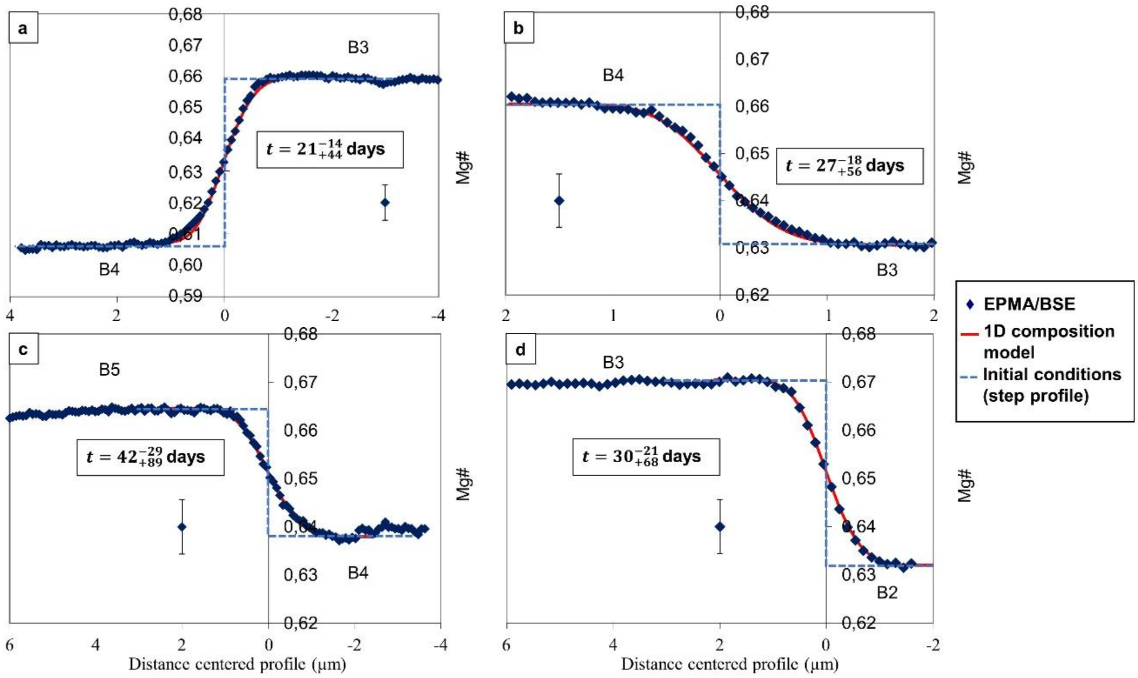

Fig. 7 Examples of best-fit models obtained after intercalibration of EMP compositional profiles and BSE grey level data of profiles in multiple-zoned orthopyroxene crystals ("B" for bands) for a temperature of 900 °C (Supplementary Table 6). a) Normal-zoned profile; b-d) Reverse-zoned profiles. Dashed lines show the initial step model used to model the diffusion timescales. Uncertainties associated to the timescales are calculated using a Monte Carlo simulation (**Supplementary Data 3**). Standard deviation on the Mg# is shown. More details in the Supplementary Materials and Supplementary Figure 3 can be found.

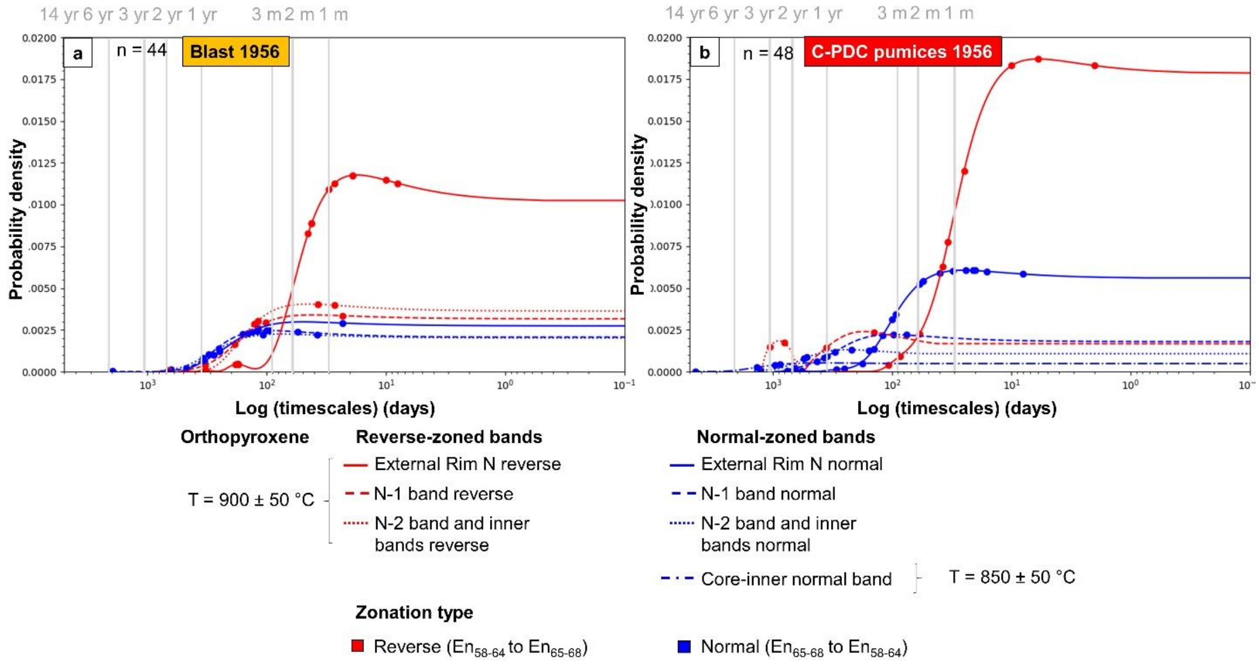

Fig. 8 Probability density functions of the Fe-Mg interdiffusion timescales for orthopyroxene crystals considering the uncertainties associated to the individual timescales. The timescales are modelled on the major compositional changes evidenced in orthopyroxene crystals depending on the location of the rim modelled in the blast (a) and post-blast C-PDC pumices (b) (normal zoning, from En_{65-68} to En_{58-64}) and then, reverse zoning, from En_{59-64} to En_{65-68}, for the inner rims, or N-1 bands or external rims N (**Fig. 5; Supplementary Data 6**). The timescales were modelled using the temperature of 900 ± 50 °C estimated by Martel et al. (accepted) for the shallow storage and 850 ± 50 °C for the core to inner normal bands. The uncertainties of the individual timescales calculations are shown in **Supplementary Fig. 12-13** and **Supplementary Data 6**. For the blast and the core-inner normal zoned band, the PDF could not be made as only one timescale was modelled on a core to inner band in a multiple-zoned crystal. n is the number of timescales modelled and N is the location of the rim. "yr" and "m" are the abbreviations of "years" and "months", respectively

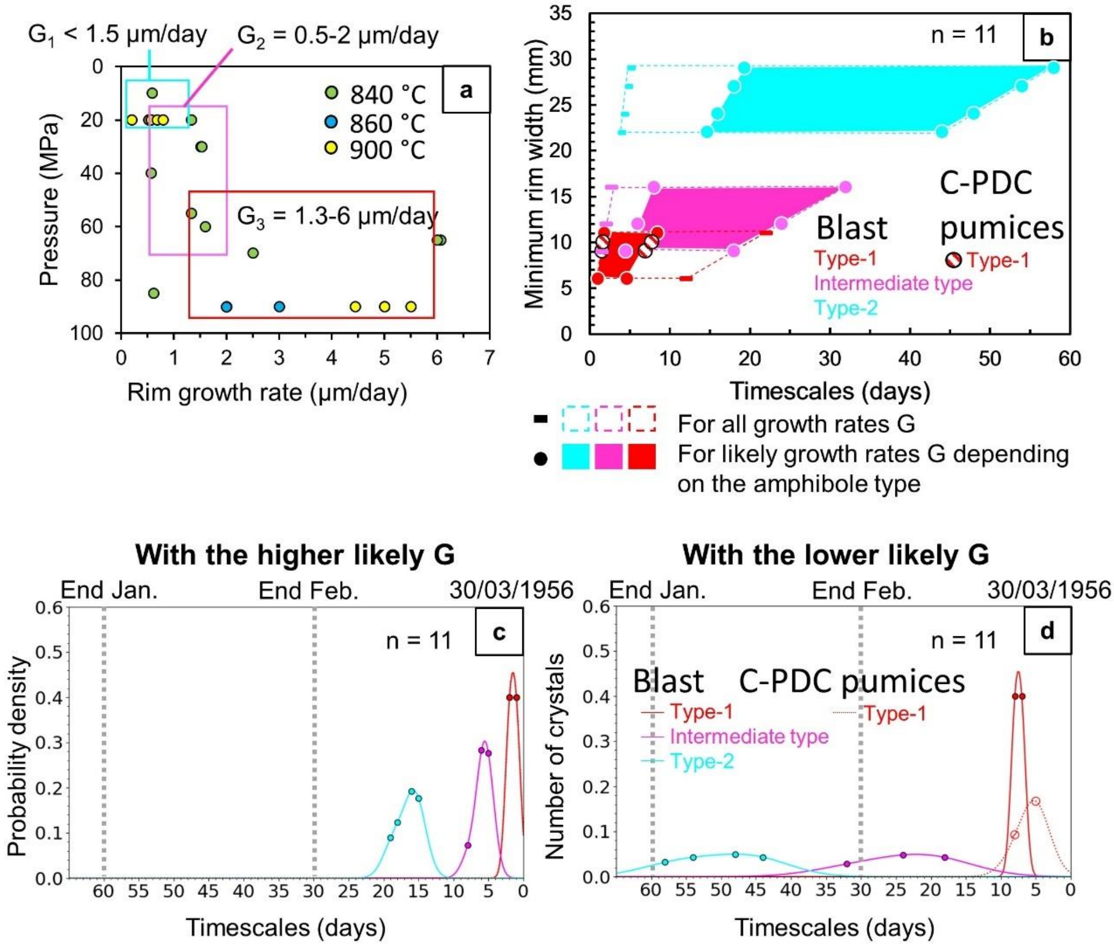

Fig. 9 Timescale constraints for the formation of amphibole decompression rims at low and very low pressures. a) Summary of decomposition rim growth rates (G) for single-step decompression experiments. Data from Rutherford & Hill (1993) for decompression experiments for 900 °C and 20 or 90 MPa (yellow symbols) and 860 °C and 90 MPa (blue symbols) and data from Browne & Gardner (2006) for 840 °C and 10 to 95 MPa. Decomposition rim growth rate decreases with decomposition pressure and temperature (as shown) and also with time (not shown). The conditions of the single-step experiments with equilibration at 90 MPa and 840-900 °C closely correspond to those estimated for amphibole decomposition in Bezymianny's system (< 100 to < 25 MPa and > 850 to ~950 °C). The experimental constraints can thus be used as constraints for the natural system, but possible small differences in temperature (e.g. possibly as high as ~950 °C in the natural system) cannot be quantified and the estimated timescales remain necessarily broad. The outlined fields mark the range of inferred equilibration pressures and probable range of decomposition rates inferred from the Rutherford & Hill (1993) and Browne & Gardner (2006) experimental data for Type-1 rims (red box), intermediate type rims (pink box), and Type-2 rims (blue box). b) Inferred shallow and very shallow amphibole residence times below the amphibole stability field for Type-1, intermediate type, and Type-2 rims for the whole range of rim growth rates ("broad estimate" in text and **Supplementary Table 4**) and for the inferred likely rim growth rates ("best estimate" in text and **Supplementary Table 4**). c-d) Probability density functions of the amphibole timescales considering the uncertainties associated to the individual timescales using (c) the higher likely growth rate or (d) the lower likely growth rate for the blast clasts and C-PDC pumices. The uncertainties on individual timescale calculations are shown in **Supplementary Fig. 13** and **Supplementary Table 4**. n in (b-d) is the number of amphibole crystals investigated

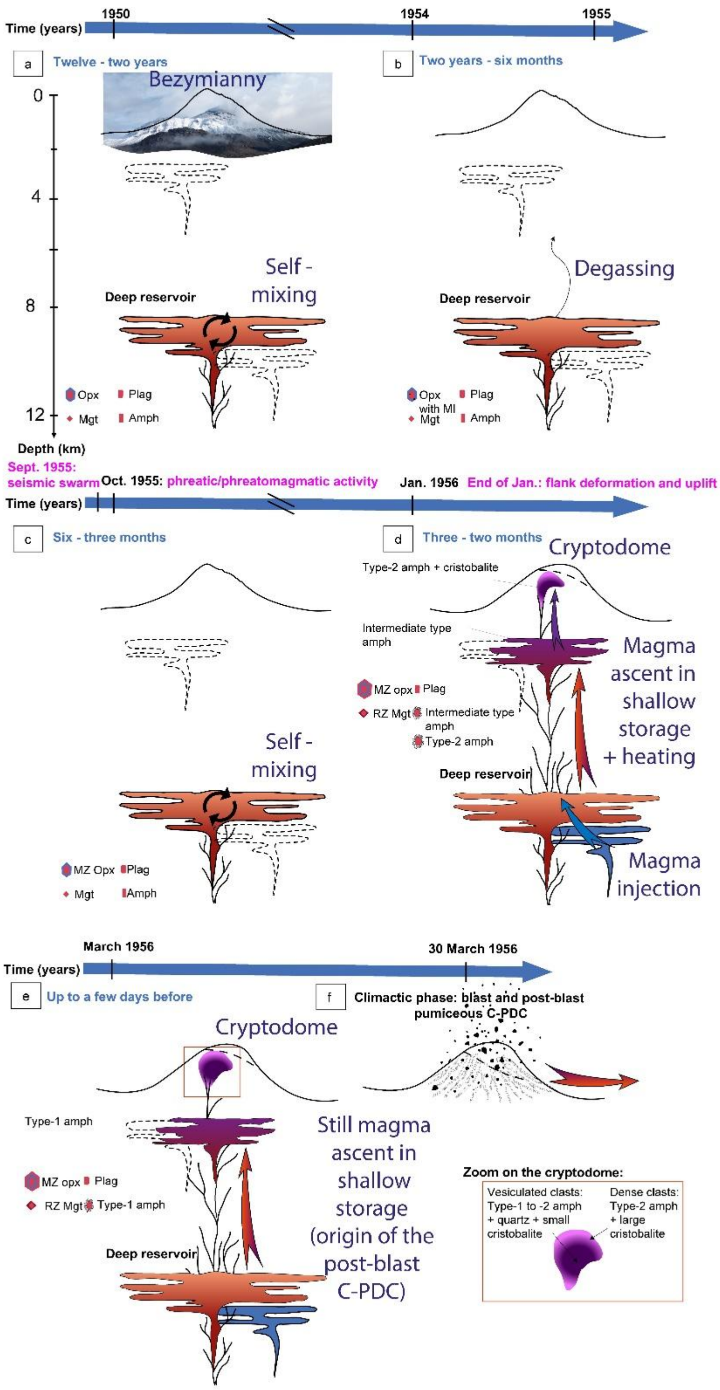

Fig. 10 Magma dynamics inferred for the 1956 climactic phase of Bezymianny from the combined point of view of orthopyroxene, magnetite and amphibole crystals in this study (Fig. 6-9), with the architecture of the magma plumbing system from Martel et al. (accepted). Geophysical observations are from Gorshkov (1959), Gorshkov and Bogoyavlenskaya (1965) and Belousov and Belousova (1998). a) Using orthopyroxene textures and timescales, we infer that self-mixing occurred in the deep reservoir several years before the climactic phase of the eruption (from reverse and normal zoning of inner bands of orthopyroxene crystals). b) Then, from 2 years to 6 months before the climactic phase, degassing of the magma occurred and formed normal zonings in orthopyroxene and recorded by melt inclusions hosted in orthopyroxene. c) Six months before, several minor orthopyroxene reverse zonings recorded self-mixing in the reservoir. d) From 3 to 2 months before, magma ascent began to

occur to form the shallow reservoir. Heating from a magma injection in the deep reservoir (Martel et al. accepted) or degassing driven crystallization with possible oxidation generated external reverse-zoned rims of orthopyroxene and magnetite and Type-2 amphibole. This mafic melt injection could have generated overpressure and favored magma ascent to the shallow reservoir (Martel et al. accepted). At the same time, the blast magma migrated to the very shallow zone forming a cryptodome (< 25 MPa) (generated from external normal-zoned orthopyroxene crystals, intermediate type amphibole and the presence of cristobalite). Normal-zoned orthopyroxene crystals from C-PDC pumices also show the beginning of magma ascent around the same time into the shallow storage zone. e) Finally, magma at the origin of the post-blast C-PDC pumices ascended in the shallow area a few days before the eruption, generating Type-1 amphibole and other amphibole crystals from the C-PDC pumices (Shcherbakov et al. 2013). f) The paroxysmal eruption of Bezymianny then occurred, on 30 March 1956, following the collapse of part of the flank of Bezymianny. Dashed outlined lenses can correspond to old, almost cooled reservoirs. “opx” stands for orthopyroxene, “mgt” for magnetite, “plag” for plagioclase and “amph” for amphibole crystals